

# Incubating Advances in Integrated Photonics with Emerging Sensing and Computational Capabilities

Sourabh Jain<sup>1,2</sup>, May H. Hlaing<sup>3</sup>, Kang-Chieh Fan<sup>1,2</sup>, Jason Midkiff<sup>3</sup>, Shupeng Ning<sup>1,2</sup>, Chenghao Feng<sup>1,2</sup>, Po-Yu Hsiao<sup>1,2</sup>, Patrick T. Camp<sup>1,2</sup>, and Ray T. Chen<sup>1,2,3\*</sup>

<sup>1</sup>Department of Electrical and Computer Engineering, University of Texas at Austin, TX 78758, USA

<sup>2</sup>Microelectronics Research Center, The University of Texas at Austin, Austin, TX 78758

<sup>3</sup>Omega Optics, Inc., 8500 Shoal Creek Blvd., Bldg. 4, Suite 200, Austin, Texas 78757, USA

\*Author e-mail address: chenrt@austin.utexas.edu

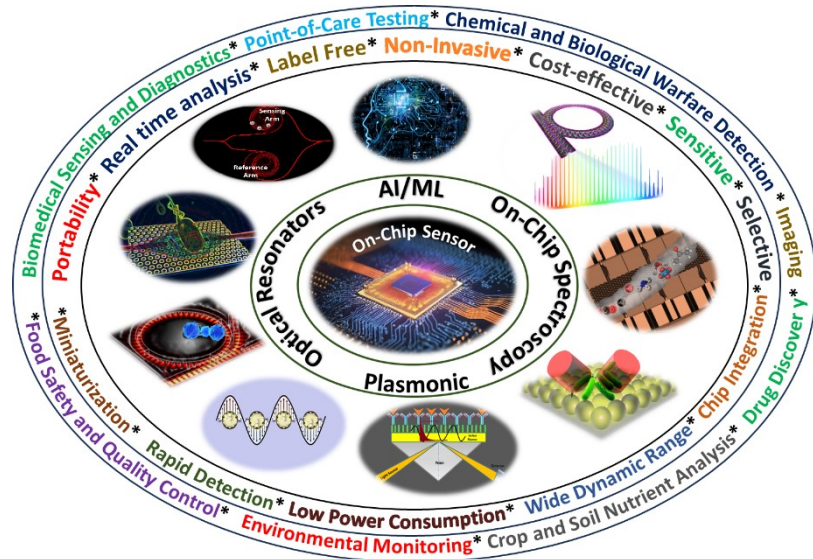
**Abstract:** As photonic technologies continue to grow in multidimensional aspects, integrated photonics holds a unique position and continuously presents enormous possibilities to research communities. Applications span across data centers, environmental monitoring, medical diagnosis, and highly compact communication components, with further possibilities growing endlessly. Here, we provide a review of state-of-the-art integrated photonic

sensors operating in near and mid-infrared wavelength regions on various material platforms. Among different materials, architectures, and technologies leading the way for on-chip sensors, we discuss optical sensing principles commonly applied to biochemical and gas sensing. Our focus is particularly on passive and active optical waveguides, including dispersion-engineered metamaterial-based structures—an essential approach for enhancing the interaction between light and analytes in chip-scale sensors. We harness a diverse array of cutting-edge sensing technologies, heralding a revolutionary on-chip sensing paradigm. Our arsenal includes refractive index-based sensing, plasmonic, and spectroscopy, forging an unparalleled foundation for innovation and precision. Furthermore, we include a brief discussion of recent trends and computational concepts—incorporating Artificial Intelligence & Machine Learning (AI/ML) and deep learning approaches over the past few years to improve the qualitative and quantitative analysis of sensor measurements.

**Keywords:** Integrated Photonics, On-Chip Sensors, Micro-ring resonators, Absorption spectroscopy, Fourier Transform Interferometer, Metamaterial, Dispersion Engineering, AI/ML Optical-Computing, Optical Neural Network, Subwavelength gratings.

## 1 Introduction to Integrated Photonics

The utilization of chip-scale photonics, governing the manipulation of photons, unlocks several unprecedented advantages, including the realm of miniaturization, amplified performance, and a broad spectrum of applications spanning communication systems, sensory mechanisms, imaging apparatuses, and quantum technologies [1–4]. Originating from the development of integrated photonics—integrating various functional devices on a chip to achieve numerous applications—has become a dominant practice



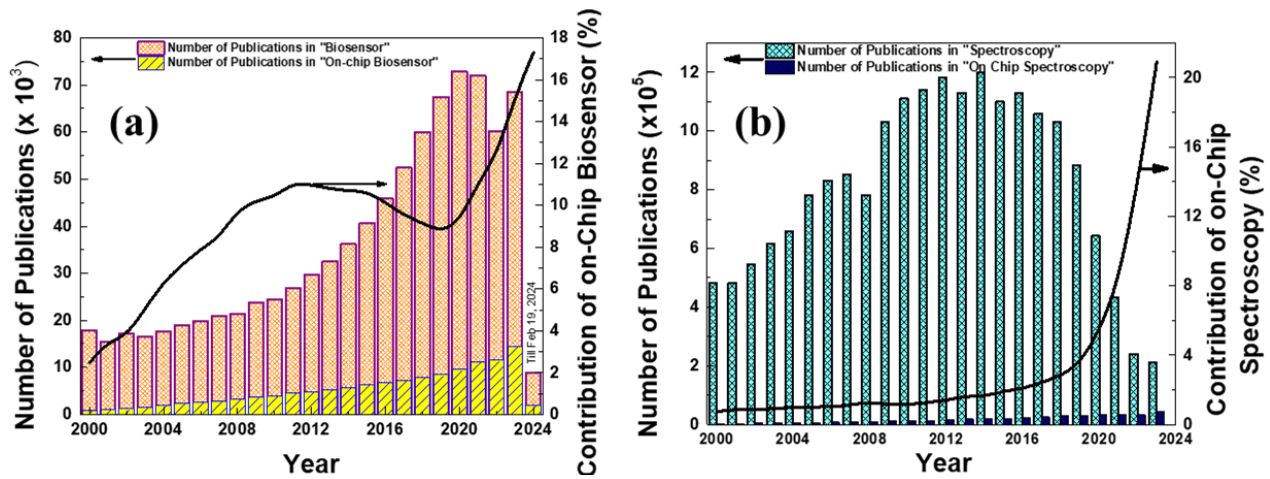


Figure 1 The publication data obtained from Google Scholar datasets over the past twenty years encompass the fields of (a) biosensors and on-chip biosensors, and (b) spectroscopy and on-chip spectroscopy.

over the past few decades. The data in Fig. 1 illustrates the advancement of on-chip biosensors and spectroscopy technologies over the last two decades, indicating the forthcoming progress in compact sensing technology [5]. In Fig.1(a), the increasing attention of researchers towards biosensors can be seen, especially the ever-increasing influence of the on-chip technique, which is a solid step toward future miniaturized and portable sensors. While Fig.1(b) shows a decline in research on spectroscopy over the past few years, despite this decline, the exponential growth in on-chip spectroscopy paves the way for ultra-small and efficient spectroscopic sensors. The compactness and scalability of integrated photonic devices have indeed made them ideal candidates. Terahertz (THz) frequencies, spanning from 10 to 750 THz and falling within the range from visible to mid-infrared on the wavelength spectrum, have garnered significant attention within the scientific community. These frequencies have been effectively transitioned to industrial-scale production for a wide range of applications [6, 7]. Depending on the operating frequencies, several material platforms and technologies have evolved during this journey [8, 9]. It is impractical to encompass all of them within a single article. This review primarily incorporates recent advancements in the most prominent on-chip technologies emerging in biochemical and gas-sensing applications, mainly on silicon (Si), silicon nitride (SiN), and indium phosphide (InP) material-based platforms.

Silicon exhibits minimal absorption across the wavelength range of 1.1-8.5  $\mu\text{m}$  and an exceptionally high refractive index of approximately  $\approx 3.4$  in this range. The most popular on-chip functions have been demonstrated on the silicon-on-insulator (SOI) platform. However, the presence of oxide in the SOI platform limits optical transparency to between 1.1  $\mu\text{m}$  and 3.8  $\mu\text{m}$  [10]. To achieve broader transparency across a range from visible to mid-infrared (approximately 300 nm to 8  $\mu\text{m}$ ), SiN has shown prominent optical characteristics. However, the refractive index is not as strong as silicon ( $<2$ ) but still satisfactory to implement numerous on-chip functionalities. Moreover, it possesses a moderately high nonlinear refractive index ( $n_2 = 2.4 \times 10^{-19} \text{ m}^2/\text{W}$ ), surpassing silica by tenfold, and crucially, it demonstrates compatibility with semiconductor mass manufacturing techniques [11].

This review article exclusively delves into on-chip biosensor devices, encompassing the incorporation of on-chip spectrometers. An optimal solution involves amalgamating sensors with the source and photodetector into a unified chip. Three fundamental strategies for harmonizing light sources and detectors with passive photonics are expounded upon. The first method, Hybrid Integration, involves integrating Photonic Integrated Circuit (PIC) or photonic device chips from various material technologies into a unified package. Executed during the packaging stage post-fabrication, it facilitates testing and

characterizes individual devices before integration, enabling meticulous selection of high-performing components and excluding non-functional ones [12]. However, a drawback lies in the larger assembly size and significant optical losses, particularly when coupling of distinct material platform-based integrated components [13]. Heterogeneous integration represents another approach, unifying various material technologies into a singular PIC chip during early fabrication. Predominantly explored for integrating III–V material into silicon [14] and silicon nitride [15], it offers advantages such as monolithic functionalities, low losses, and reliable performance. However, challenges include the inability to perform component-by-component testing in processes like die-to-wafer bonding, necessitating precise optical alignments and intricate packaging. The final approach includes monolithic integration, entails fabricating passive photonics and lasers/detectors on a bonding-free single epitaxially grown platform. In sensing applications, integrating a source and detector alongside chip-based sensing elements consistently emerges as the preferred approach among these techniques. Despite their indirect bandgap semiconductor status, Si and SiN platforms face limitations in integrating on-chip sources and detectors, impeding the realization of fully functional devices. III-V material systems, particularly centered on the InP-based platform, exhibit great potential for designing fully functional lab-on-chip spectrometers. Notably, the InP platform has demonstrated efficacy in source-detector integration at room temperature, offering extensive wavelength coverage from near-infrared to mid-infrared regions. It's worth mentioning that InGaAs core and InP cladding materials exhibit minimal material losses, measuring less than 2 dB/cm within the wavelength range of 3-15  $\mu\text{m}$  [16].

Within the framework of the platforms mentioned in the preceding paragraph, regarding technologies employed in on-chip bio-sensing applications, and our primary focus will be advancements in refractive index sensing. More specifically, we will explore cutting-edge innovations involving micro-ring resonators and biosensors rooted in photonic crystals. Furthermore, we will illuminate the recent strides made in plasmonic-based sensing, considering resonances in both propagating and localized surface plasmons, as well as the popular spectroscopic technique that exploits plasmonic resonances known as surface-enhanced Raman spectroscopy. On a different note, when discussing gas sensing applications, our examination will be centered on the developments and achievements in on-chip absorption spectroscopy. Notably, we will place particular emphasis on the Mid-IR region, which has garnered substantial scientific interest in the presence of the fundamental absorption signatures for the majority of gas molecules within this spectral realm. We will also briefly touch upon recent advancements in various spectroscopic techniques, including Fourier Transform Interferometer Spectroscopy, Frequency comb spectroscopy, and Wavelength modulation spectroscopy. Lastly, we will delve into integrating artificial intelligence and machine learning techniques to enhance the analysis and predictive capabilities followed by the concluding remarks.

## **2 Refractive Index based-Sensing**

The refractive index is a fundamental material property that dictates the electrical, optical, and magnetic characteristics and behavior of a device. Depending on the composition, geometry, and operating wavelength, optical waves propagating in the core guiding medium surrounded by cladding experience an average refractive index, often referred to as the effective refractive index ( $n_{\text{eff}}$ ) of the propagating mode. The chip-level manipulation of  $n_{\text{eff}}$  has been extensively exploited to alter photon behavior, resulting in many exciting engineered optical properties that can be employed for various applications, including sensing and computing [17–20]. In biosensing, the change in  $n_{\text{eff}}$  of the waveguide can be used to detect changes in the refractive index of the surrounding medium, often indicative of changes in the physical properties of the medium, such as the presence of biomolecules or the occurrence of biochemical reactions. Evanescent coupling mechanisms are counted among very effective sensing methods and are

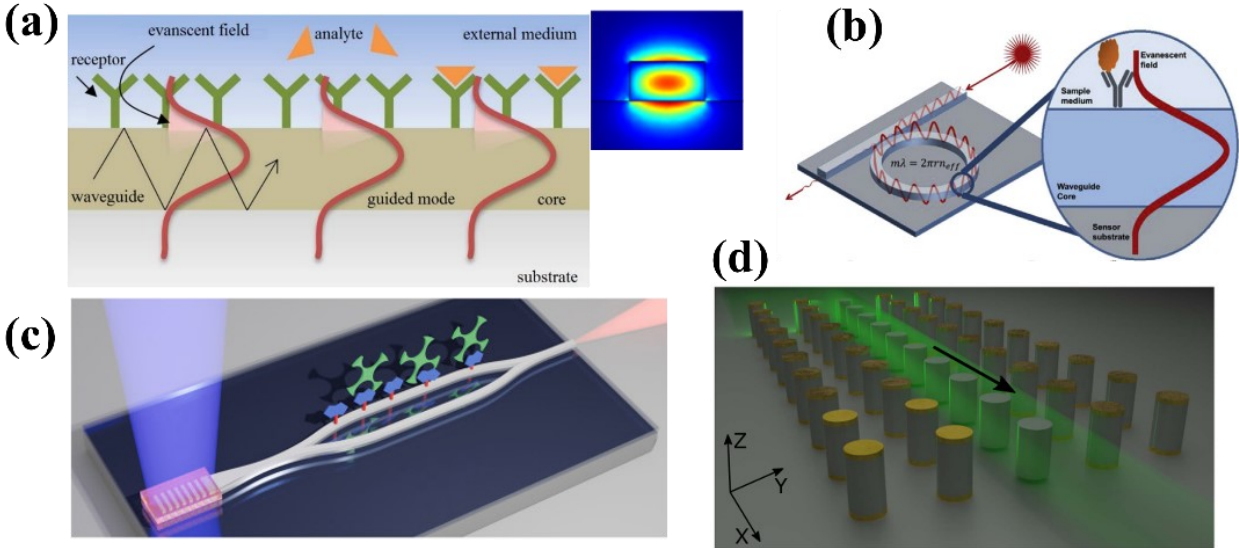


Figure 2 Exemplary artistic view of optical evanescent coupling in different optical structures. (a) The optical waveguide, accompanied by an inset displaying the optical mode profile, demonstrates the presence of an evanescent tail in the cladding (bottom) and external medium [21]. In (b), the evanescent wave extending from the micro-ring resonator waveguide probes the local refractive index [22]. (c) Mach-Zehnder interferometer sensing configuration where one arm of the MZI is open to interact with the sensing molecule and another arm acts as a reference arm [23]. In (d), an illustration depicts the defect mode Photonic crystal waveguide situated in the central row within the waveguide [24].

most prominent at the on-chip miniaturized scale, easily fabricated using a mature microfabrication process flow. The evanescent field sensing technique utilizes planar and resonator waveguiding structures that permit the electromagnetic field to extend beyond the device surface, enabling interaction with analyte molecules or biomolecules in close proximity. When an analyte contacts the evanescent tail, it changes the  $n_{eff}$  of the propagating optical mode. Information about targeted analytes can be extracted by tracking the fundamental properties of the propagating signal (i.e., intensity, phase, and polarization). Researchers have explored different structural geometries, with micro-ring resonators (MRRs), Mach-Zehnder interferometers (MZIs), photonic crystals, and plasmonic structures emerging as the most extensively studied and well-known options. Fig. 2 shows the evanescent coupling mechanism in various standard optical waveguide configurations.

## 2.1 Micro ring resonator

Optical micro-ring resonators are highly sought-after devices with potential applications in various fields, including telecommunications, sensing, and biomedical imaging [25–27]. The fundamental working principle of optical micro-ring resonators involves the interference of light waves propagating around a ring-shaped waveguide. Resonant coupling occurs when the circumference of the ring is an integer multiple of the wavelength of light, leading to constructive interference and a decrease in transmission at the resonant wavelength at the through port [28]. The resonant wavelength depends on factors such as the ring's radius, the refractive index of the material, and the number of times the wave propagates around the ring. These resonant properties can be modified by adjusting these parameters.

In this section, we present a comprehensive overview of recent advances in optical micro-ring resonators for sensing applications, emphasizing their performance, selectivity, and sensitivity. We also address challenges and opportunities for future development. Optical micro-ring resonators have shown promise in biosensing applications as label-free biosensors for detecting biomolecules. The binding of a biomolecule to the ring's surface alters the effective refractive index ( $n_{eff}$ ) of the device, resulting in a

shift in the resonant wavelength. This shift can be quantified and correlated with the concentration of the

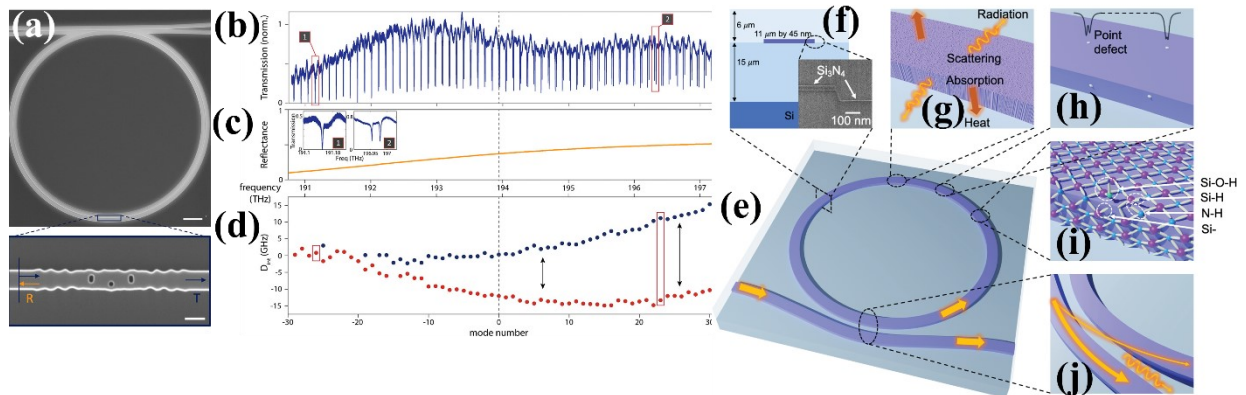


**Figure 3** High  $Q$  engineered ring-resonator, (a) A SEM image depicting fabricated silicon micro-ring resonator featuring a partially reflective component within the structure, (b) transmission spectrum demonstrating the presence of the inverse designed intracavity element, (c) calculated reflectance spectrum exhibiting an increase in reflectance as the frequency rises, (d) The integrated dispersion of the split fundamental modes illustration, with blue and red points denoting each side of the split modes. (a-d reproduced from [27]) (e) Illustration image of ultra-high  $Q$  MRR. (f) The cross-section waveguide image with an SEM image (inset). The cross-section exhibits bottom cladding, a silicon nitride waveguide core grown through etched low-pressure CVD, an additional thin layer of SiN lids the sidewalls and top of the core, and a top cladding of oxide formed. (g) Scattering via rough surface of waveguide causing radiation mode, while bulk absorption results in heat. (h) Resonances experience splitting due to point defects. (i) Surface absorption occurs as a result of defect bonds such as Si-O-H, Si-H, N-H, and dangling bonds. (j) The bus-ring coupler serves the dual function of dispersing energy into radiation modes and inducing additional loss. (e-j reproduced from [26]).

biomolecule.

Achieving high sensitivity in simple ring resonator-based devices (without any index perturbation) on commonly used Si, SiN, and InP-based material platforms is challenging. This challenge arises due to the limited mode overlap of the evanescent field with the analyte, a small footprint area, background noise, and unavoidable material losses. Several key approaches can be employed to enhance the sensing performance of a ring resonator-based on-chip device. Optimizing the ring resonator design and improving the signal-to-noise ratio (SNR) can offer low optical losses and an exceptionally high-quality factor (Q-factor) of the resonator. For instance, Ahn et al. experimentally achieved an extraordinary quality factor exceeding 2 million on a SOI platform, employing single-mode operation and selective manipulation of wavelength bands through flexible dispersion engineering in the MRR, using an inverse design approach (see Fig. 3(a-d)) [27]. In another example, Puckett et al. [26] presented a  $Si_3N_4$  resonator with exceptionally high intrinsic quality factors of 422 million and an absorption-limited Q of 3.4 billion through careful reduction of scattering and absorption losses. They demonstrated narrow linewidths, with an intrinsic linewidth of 453 kHz and a loaded linewidth of 906 kHz with a remarkably low loss of 0.060 dB/m (see Fig. 3(e-j)). Employing noise reduction techniques like temperature stabilization and shielding can further increase sensitivity while maintaining reliable device operation [26, 29–31].

Another approach involves modifying the waveguide or ring resonator surface to enhance light-matter interaction, incorporating sub-wavelength gratings and photonic crystal cavities to improve sensitivity further [22, 32–35]. Recently, our group experimentally demonstrated a subwavelength grating MRR to detect SARS-CoV-2 by functionalizing the sensing surface. We successfully detected and differentiated CoVID-19 and influenza with a remarkable detection limit of 100 fg/ml [36] (Fig. 4 (a)-(c)). The exceptional performance can be attributed to the optimized rectangular silicon pillars comprising sub-wavelength gating micro-ring resonators (R-SWGMRs), creating an asymmetric effective refractive index

distribution and significantly reducing bending loss. In another biosensing example, trapezoidal-shaped ring pillars were optimized, and 1nM miRNA with anti-DNA: RNA antibody amplification was observed [37], aided by the significantly reduced bending loss in the ring structure [38, 39] (Fig. 4 (d)-(g)).

Similar to the subwavelength grating structure, incorporating photonic crystals in the ring structure can enhance light-analyte interaction, as discussed earlier. A work presented by Sun et al. [40] explored a one-dimensional photonic crystal micro-ring resonator (PhcMRRs) operating within the high-order photonic bandgap in the mid-infrared range. This resonator demonstrated enhanced field confinement in the analyte, benefiting from a slow light assistance structure. A similar approach is used by Wang et al. [41] using two cascaded silicon-on-insulator PhcMRRs employed for dual-parameter sensing utilizing a multiple resonances multiple modes technique. This approach simultaneous humidity and temperature measurement with a single-spectrum measurement. The obtained results included a relative humidity (RH) sensitivity of 3.36 pm/%RH and 5.57 pm/%RH, along with a temperature sensitivity of 85.9 pm/°C and 67.1 pm/°C for the selected dielectric mode and air mode, respectively (Fig. 4 (h),(i)) [41]. Subsequently, a significant enhancement in both volumetric and surface sensing sensitivity has been demonstrated with a sensitivity of approximately 248 nm/RIU for the detection of DNA and proteins at the nanomolar level, representing more than a two-fold improvement compared to conventional MRR (Fig. [35]).

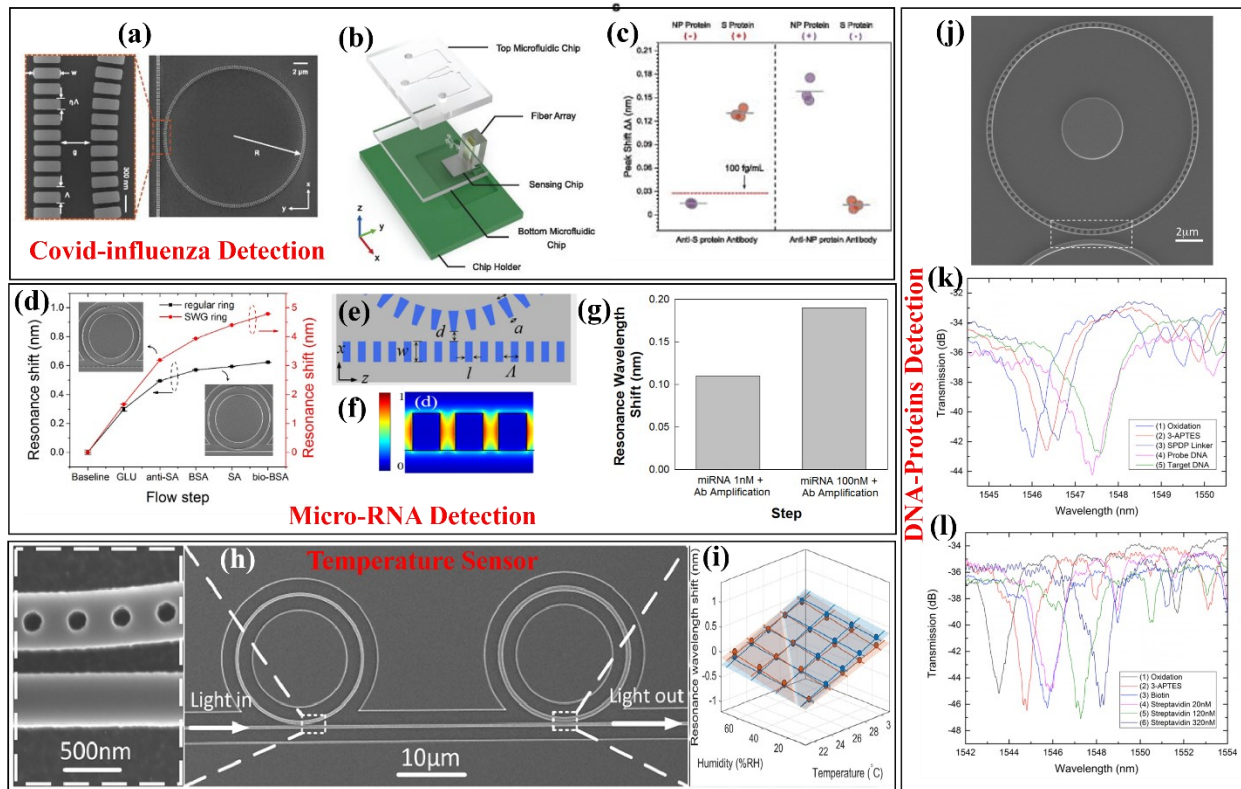


Figure 4 Numerous applications experimentally demonstrated on the index-perturbed micro-ring resonator platforms. (a) SEM image of the subwavelength grating micro-ring resonator. (b) Virtual representation of the biosensing platform in an exploded manner. (c) Testing for cross-reactivity between SARS-CoV-2 and influenza ((a)-(c) reproduced from [36]). (d) The shift in resonance in unperturbed and perturbed MRRs during the sequence of layer functionalization to detect micro-RNA. (e) Trapezoidal-shaped ring schematic and electric-field distribution of the optical mode in the bus waveguide (f). (g) Experimental validation of micro-RNA on the chip ((d)-(g) reproduced from [37]). (h) SEM image of two cascaded photonic crystal micro-ring resonators. (i) Measured and predicted resonant wavelength shifts under different humidity and temperature conditions ((h),(i) reproduced from [41]). (j) SEM image of photonic crystal micro-ring resonator. (k) and (l) Experimental demonstration of DNA and protein detection, respectively ((j)-(l) reproduced from [35]).

Table 1 summarizes experimental bio-sensing results across various applications, highlighting key performance parameters. It is evident that the incorporation of subwavelength gratings (SWG) significantly enhances sensitivity, primarily due to the expanded surface area and improved light-analyte interaction.

Among several other methods, the hybrid integration of on-chip components with nanoparticles can enhance sensitivity and the local electromagnetic field [42–44]. On-chip signal processing techniques, including filters and amplifiers, improve signal quality and reduce noise. Exploring novel material platforms like 2D materials [45–48] and nanocomposites also enables new sensing functionalities [49]. Kou et al. [48] presented an innovative approach to detect dopamine neurotransmitters by utilizing graphene integrated into a silicon micro-ring resonator structure. This design, incorporating Si-based waveguides and ring resonators, offers the benefit of a compact sensing surface area of  $30\mu m^2$ . The experiments were carried out at telecom wavelengths. However, for enhanced detection of biologically significant molecules, the utilization of mid-IR wavelengths could lead to substantial advancements. In this regard, several studies have explored the potential of waveguide-integrated graphene chemical sensors designed explicitly for mid-IR operation [50, 51].

Table 1: Comparative analysis of bio-sensing performance verified through experiments across a variety of applications.

MRR type	Q-Factor	Sensitivity	Application
Strip Waveguide	20000	70 nm/RIU	Protein detection [52]
Ultra-thin Rib Waveguide	25000	100 nm/RIU	Temperature detection [53]
Rectangular SWG	1200	248 nm/RIU	DNA and protein [35]
Rectangular SWG	2180	423 nm/RIU	Streptavidin [54]
Rectangular SWG	1650	437.2 nm/RIU	SARS-CoV-2 [36]
Trapezoidal SWG	9100	440.5nm/RIU	miRNA [37]

## 2.2 Photonic crystal-based biosensor

Photonic crystal waveguides have emerged as a pioneering breakthrough in the realm of photonics, offering distinctive characteristics and an array of applications. These waveguides operate on the principle of manipulating light propagation by introducing periodic variations in the refractive index within a dielectric structure. Bragg reflection and defect band-guided propagation represent two distinct wave propagation modes in photonic crystal waveguides. Bragg reflection relies on the periodic variation of the refractive index in the waveguide causing wave reflection of specific wavelengths while allowing others to pass through. In contrast, defect band-guided propagation involves an ingenious mechanism that creates a photonic bandgap, a range of wavelengths where light is forbidden to propagate, resulting in controlled and confined light guidance. In addition to applying refractive index sensing as discussed earlier in the context of Micro-Ring Resonators, a similar approach can be employed on the platform of photonic crystal waveguides using both the propagation mechanisms. Furthermore, by employing bandgap engineering techniques, PCWs can be utilized to achieve the desirable properties of slow-light-induced light dispersion, which form the foundation of absorption spectroscopy beneficial for gas sensing applications. These aspects will be elaborated upon in the corresponding section (section 4.1), providing a detailed exploration of their significance.

The advent of photonic crystal waveguides has revolutionized various fields, particularly the field of biochemical and gas sensing applications [55–60]. By incorporating functional materials or employing surface modifications within the waveguide, an exceptional level of sensitivity to the surrounding

environment is achieved. This heightened sensitivity facilitates precise detection and analysis of biochemical substances and gases. The dominance of one-dimensional (1D) [61–64] and two-dimensional (2D) [65] photonic crystal waveguides (PCWs) arise from their extensive utilization compared to three-dimensional (3D) PCWs [66]. This preference can be attributed to the increased design flexibility and the ease with which they can be integrated with other photonic components, making them highly versatile and practical options in the field of photonics. The compact dimensions, heightened sensitivity, and seamless integration capabilities position photonic crystal waveguide as an alluring platform for biochemical sensing. They have exhibited remarkable capabilities in the detection of biomolecules such as DNA, proteins, and chemical markers, demonstrating elevated levels of specificity and sensitivity. The confinement of light within the waveguide engenders pronounced interactions with the analytes, leading to augmented sensing performance.

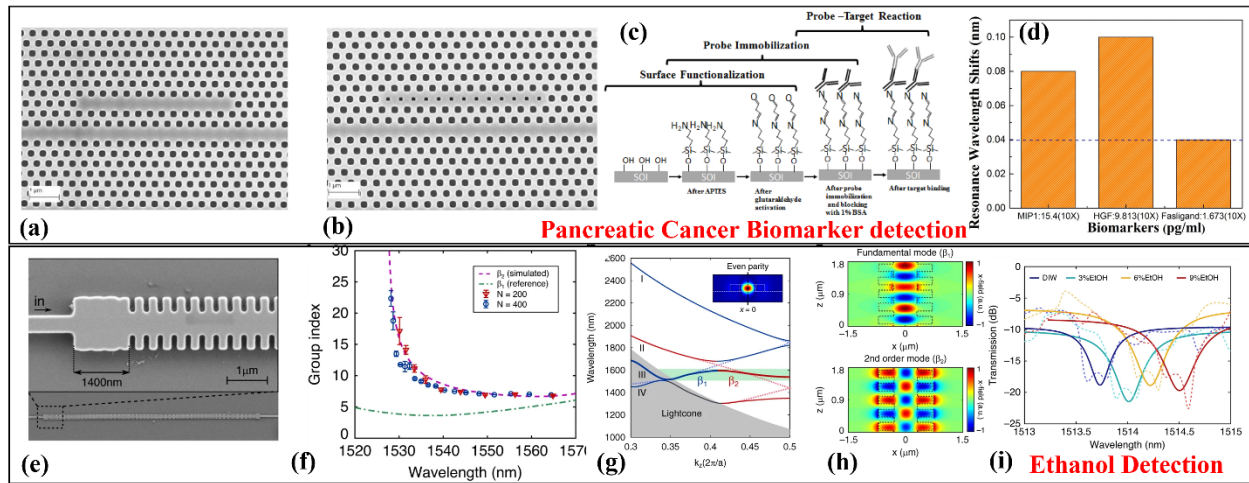


Figure 5 Exemplary Photonic Crystal Biosensors from Published Studies: (a) SEM images of an L13 PC microcavity, (b) L13 PC microcavity with nanoholes, (c) Chemical structure involved in the biosensing reaction for detection of pancreatic patient plasma, (d) Resonance shift observed for three biomarkers (Fasligand, MIP1, HGF) ((a)-(d) reproduced from [60]) (e) SEM image of a 1D photonic crystal waveguide, focusing on single-mode and bimodal sections, (f) Experimental group index data were acquired from interference points, utilizing the simulated fundamental mode group index as a reference, (g) a dispersion diagram illustrating the first 3 x-even parity bands for TE-like polarization, (h) real part of the electric field's x-component for both the fundamental and higher-order modes, (i) Experimental optical spectra with different concentrations of ethanol in Deionized Water. ((e)-(i) reproduced from [61]).

By leveraging the defect-guided bandgap effect in photonic crystal waveguides (PCWs), Yang et al. [60] effectively identified three distinct biomarkers present in the plasma of individuals with pancreatic cancer. (Fig. 5 (a)- (d)). Detection was accomplished through conventional L13 defect-engineered microcavities lacking nanoholes (Figure 5(a)), and with increased sensitivity, utilizing L13 PC microcavities featuring nanoholes (Figure 5(b)). Remarkably, the experimental setup detected a concentration as low as 8.8 femtomolar (334 fg/mL) of the targeted biomarker in the plasma samples of patient, it corresponds to a 50-fold dilution compared to ELISA. Despite the extraordinarily engineered optical behavior in a miniaturized chip scale, the PCW-based structure is sometimes incompatible with other integrated optical structures, complicating the mass-manufacturing process [67]. Torrijos et al. [61] significantly addressed the incompatibility problem by utilizing a 1-D PCW. They reported the first instance of slow light bimodal interferometric behavior within an integrated single-channel 1D-PCW and also demonstrated ethanol sensing (Fig. 5 (e)-(i)). Among the several bio-chemical sensing, gas sensing is not well suited to the on-chip refractive index-based method primarily due to limited sensitivity and selectivity to gas



molecules as gas molecules have a negligible change in the refractive index compared to other fluid analytes and surrounding air cladding. However, plasmonic structures can enhance the interaction between light and gas analytes, and thus have the potential to address the issues faced by conventional refractive index sensors as discussed in the next section (Section 3). Table 2 presents empirical findings on the performance of biosensors across a spectrum of applications. Of particular note is the relatively limited number of experimental demonstrations in the realm of two-dimensional Photonic Crystal Waveguides, despite the wealth of theoretical research highlighting their potential utility in biosensing. The lack of experimental validation is mainly due to the complex and fragile attributes of 2D PCWs. These characteristics impose strict limitations on fabrication flexibility and make device features highly sensitive to even minor variations in the fabrication process. Conversely, there has been a recent surge of interest in 1D-PCW. Notably, the deliberate engineering of multimodal interference via dispersion-engineered phenomena holds significant promise for developing high-performance biosensors in future research and innovation.

*Table 2: A tabulated compilation of experimentally confirmed performance results using photonic crystal waveguides in diverse applications for biosensing.*

Device type	Q-Factor	Sensitivity	Application
L13 defect hexagonal 2D PCW	22000	112nm/RIU	Pancreatic cancer biomarker detection [60]
L3 defect hexagonal 2D PCW	26760	15ng/ml	Antibodies detection [68]
Slotted hexagonal photonic crystal	4000	500nm/RIU	Avidin/biotin detection [65]
Line defect hexagonal 2D PCW		94.2 pm/ $\mu$ M	DNA detection [69]
1D Biomodal PCW		150.83 $2\pi$ rad/RIU	Ethanol detection [61]
1D Asymmetric multimode PCW	861	325nm/RIU	NaCl detection [62]

### 3 Plasmonic-based On-Chip Sensing

Plasmonic is a field of study that focuses on the interaction between light and free electrons in metals, specifically the collective oscillations of these electrons known as plasmons [70–72]. Plasmonic phenomena occur when light interacts with nanoscale metallic structures, enabling the manipulation and confinement of light at subwavelength scales. This unique capability of plasmonic structures has paved the way for numerous applications, particularly in the realm of on-chip sensing. We will discuss different types of plasmonic-based sensors in the subsequent subsections.

#### 3.1 Surface plasmon resonance sensor

Surface plasmon resonance (SPR) sensors are advanced optical devices employed for highly sensitive molecular interaction analysis on sensor chips [73, 74]. These sensors exploit the surface plasmon resonance phenomenon, which involves the collective oscillation of free electrons at the interface of a metal (typically gold or silver) and a dielectric medium. By directing a light beam onto this interface at a specific resonance angle, the absorption of light by plasmons occurs, resulting in a distinct dip in reflected light intensity. This dip, exquisitely responsive to refractive index changes near the metal surface, serves as a reliable indicator of binding or dissociation events between molecules of interest. Immobilizing one binding partner on the metal surface enables real-time monitoring of molecular interactions by measuring shifts in the resonance angle or reflected light intensity. SPR sensors find diverse applications in fields

such as biochemistry, pharmaceuticals, and environmental monitoring, offering label-free detection, real-time analysis, and multi-interaction capabilities [75–77].

Chip-based SPR sensors offer several advantages, including label-free detection, dynamic measurement of binding kinetics, and high sensitivity. However, standard SPR chips have limitations such as restricted polarization compatibility, low selectivity, and shallow penetration depth. Modifications like long-range SPR chips have been developed to overcome these challenges [78, 79], enabling deeper penetration and specific sensing of larger bio-entities. These advancements enhance the capabilities of chip-based SPR sensors, expanding their potential for diverse applications. SPR excitation necessitates a coupling medium to impart photon momentum at the interface, which can be accomplished through high-index prisms, gratings, waveguides, or optical fibers [75]. Grating-coupled structures were introduced in SPR on-chip devices to enable miniaturization and integration within lab-on-a-chip systems. However, grating-coupled

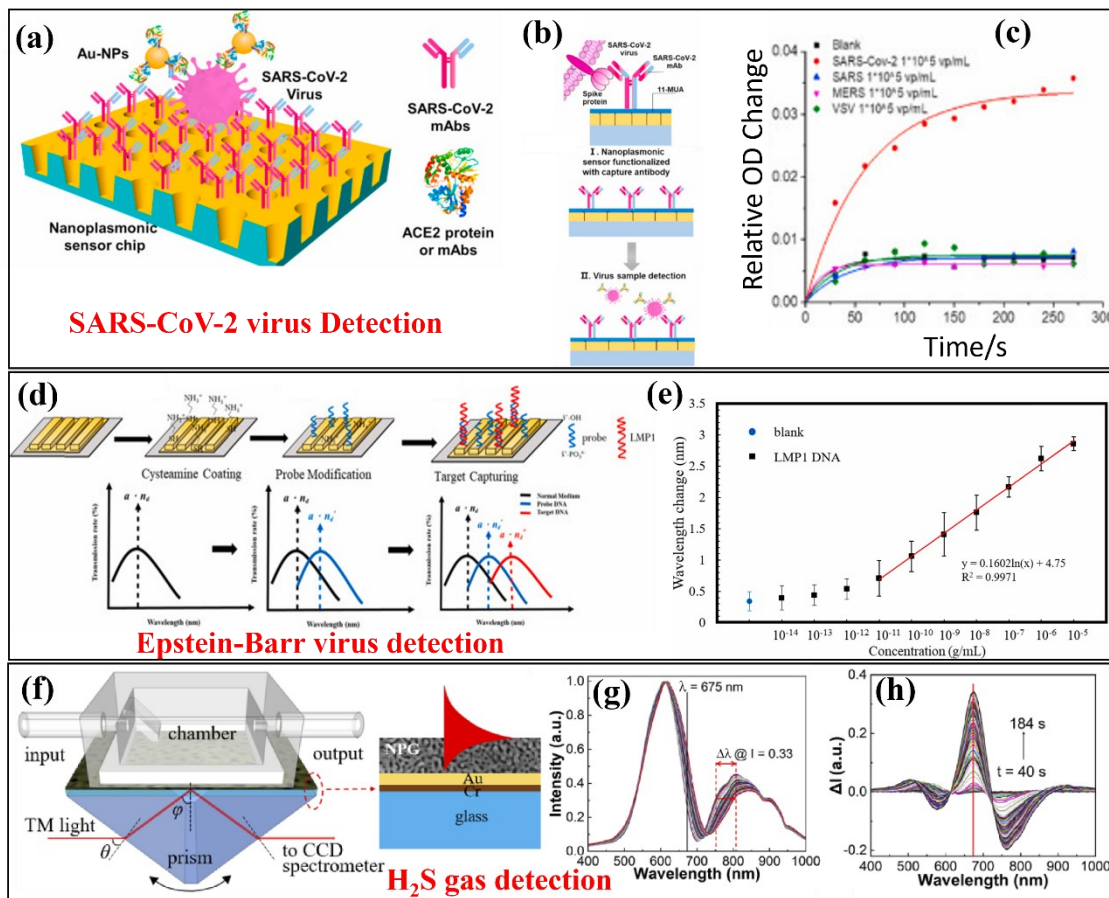


Figure 6 State-of-the-art experimental demonstrations utilizing Surface Plasmon Resonance phenomenon. (a) Schematic of plasmonic nano-cup array sensor. (b) The diagram illustrates the interaction between the spike protein situated on the surface of the SARS-CoV-2 virus and the respective monoclonal antibodies targeting SARS-CoV-2. (c) Testing the specificity of AuNP-elevated virus detection: Dynamic binding curves of SARS-CoV-2 antibodies with various SARS-CoV-2, SARS, MERS, and VSV pseudo viruses at  $1.0 \times 10^5$  vp/mL concentration. ((a)-(c) are reproduced from [89]) (d) Gold capped nano-slit SPR chip layer functionalization with a probe for DNA detection, (e) The calibration curve for latent membrane protein 1 sensing is presented using the continuous microfluidic PCR integrated nano-slit-SPR sensor. ((d), (e) are reproduced from [90]). (f) Depiction of the Kretschmann-type spectral NPG-SPR sensor platform for in situ gas detection at room temperature. (g), (h) Spectra of reflected light intensity were recorded at various time points following the introduction of 100 ppm H<sub>2</sub>S gas and diverse spectral variations compared to the resonance spectrum captured at 40 seconds respectively. ((f)-(h) reproduced from [91]).

SPR systems face limitations due to lower sensitivity than prism-coupled systems. To overcome the issue, Rossi et al. [80] integrated sensing areas with gratings in microfluidic chambers and achieved a 30-50% increase in the global response, making the grating coupler more competitive.

SPR on-chip is extensively used in biomedical research for studying protein-protein interactions [81], DNA hybridization [82], and ligand-receptor binding [83]. Additionally, SPR-based biosensors are also popular for clinical diagnostics to detect and quantify biomarkers related to various diseases, such as cancer [84–86], infectious diseases, viruses [87], and cardiovascular disorders [88]. A cost-effective and efficient SPR device was developed by Huang et al. [89] to sense the SARS virus in one shot. By combining a nano-plasmonic biosensor with a standard 96-well plate or chip cartridge, the device achieved rapid detection (<15 min) with high sensitivity (limit of detection = 370 viral particles/mL), directly detecting the entire virus (Fig. 6(a)-(c)). In another approach to COVID-19 detection, Basso et al. [92] achieved successful detection of SARS-CoV-2 antibodies in the serum of patients through SPR utilizing Au-SPR chips functionalized with self-assembled monolayers (SAMs). Recently, Hsieh et al. [90] introduced a practical approach that integrated microfluidic polymerase chain reaction (PCR) with an SPR sensor based on gold nano-slits. This method was employed for the detection of the DNA sequence associated with latent membrane protein 1 (LMP1) (Fig 6(d)-(e)). In addition to the biosensing applications, SPR chip-based platforms are also gaining much interest in gas sensing applications [93–95]. Liu et al., [91] demonstrated gas sensing application in a Kretschmann-type spectral nano-porous gold (NPG)-SPR sensor using a 60-nm-thick NPG film. It was tested for its response to toxic  $H_2S$  gas at room temperature. By adjusting the dealloying time to control film porosity, the sensor achieved its optimal sensitivity to  $H_2S$ . Compared to a conventional Au-SPR sensor, the NPG-SPR sensor showed at least six times higher sensitivity to 100 ppm  $H_2S$  (Fig. 6 (f)-(h)).

### 3.2 LSPR-Based Sensor

Localized Surface Plasmon Resonance (LSPR), a subtype of Surface Plasmon Resonance (SPR), shows promise as a highly sensitive technique for plasmonic biosensing. LSPR is characterized by the confinement of the resonant electromagnetic (EM) field within a metallic nanostructure, allowing it to detect changes in the refractive index of the surrounding medium within a short distance of a few tens of nanometers. Scattering and absorption effects dominate when dealing with colloidal nanoparticles exhibiting random orientations. Mie theory offers a framework for analyzing the extinction cross-section (incorporating absorption and scattering) of a metallic nanosphere characterized by radius  $R$  and dielectric constant ( $\epsilon_m$ ), surrounded by a dielectric material ( $\epsilon_d$ ).

$$\sigma_{ext} = 12 \frac{w}{c} \pi \epsilon_d^{3/2} R^3 \frac{Im(\epsilon_m)}{[Re(\epsilon_m) + 2\epsilon_d]^2 + [Im(\epsilon_m)]^2} \quad (1)$$

Typically, LSPR sensors are created by constructing metallic nanostructures like nanospheres, nanorods, nano-shells, nanowires, and nano-prisms, along with an additional sensing film layer. The efficiency of electrolysis enhancement and light quenching in LSPR is greatly influenced by the proximity, size, shape, and material of the nanoparticles. As a result, precise control over the size and shape of the nanoparticles is necessary to achieve the desired optical response [96, 97]. Progress in nanolithography techniques has enabled the accurate fabrication of such nanostructures on substrates, thereby enabling the utilization of LSPR-based sensors with colloidal particles and miniaturized chip-based substrates. These chip-based substrates offer high sensitivity, repeatability, and the capability to function with other sensing systems like microfluidics [87, 98].

LSPR is utilized for transmission measurements, while SPR detects changes in reflectance when a material is attached to a single particle [99, 100]. The primary advantage of LSPR is the simplified

construction of the measurement system, as it eliminates the requirement for movable elements needed in reflection angle measurements. The transmissive signal response has found applications in diverse biomolecule detection scenarios by observing the plasmon peak shift in nanoparticle sensors, contrasting with LSPR-based reflective signal sensors [101].

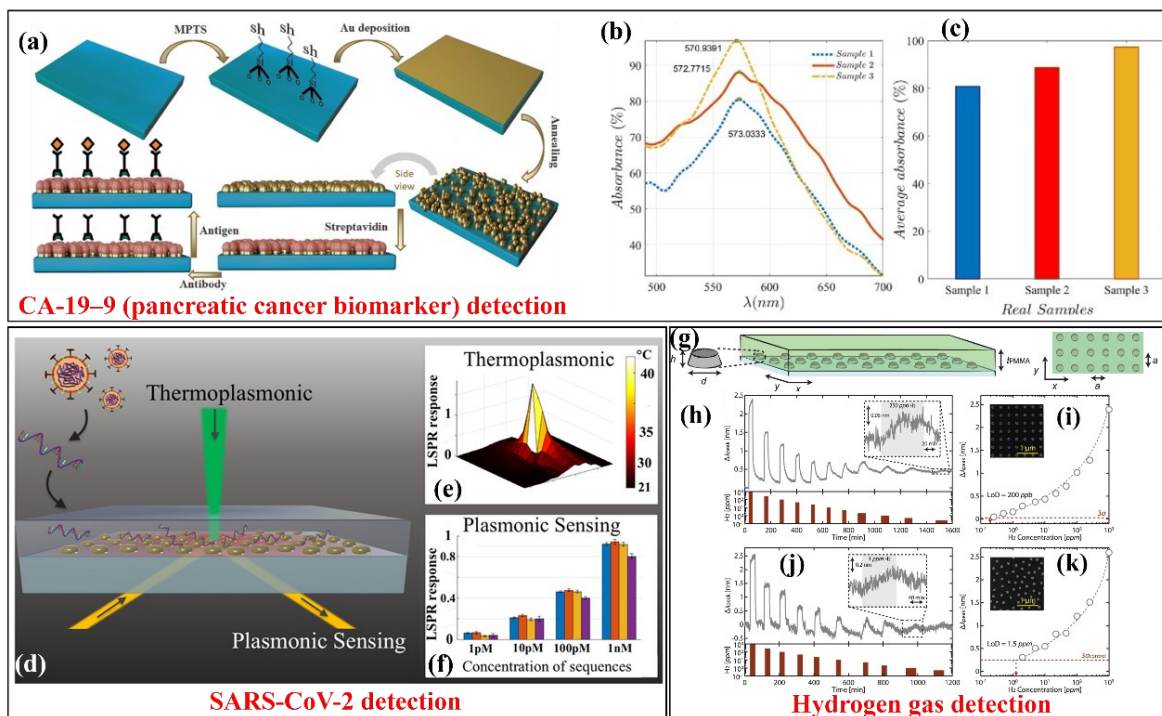


Figure 7 Cutting-edge experimental applications exploring the Localized Surface Plasmon Resonance phenomenon. (a) Stepwise preparation of a gold nanoparticle array on the glass substrate. (b), (c) Detection of Carbohydrate antigen 19-9 (CA-19-9) in three different samples. ((a)-(c) are reproduced from [102]). (d) Schematic of Plasmonic photothermal enhanced LSPR sensor. (e) Thermal map distribution around the photothermal heat source. (f) Quantifying viral oligos with dual-functional LSPR biosensors ((d)-(f) are reproduced from [103]). (g) Schematic of the palladium nanoparticles periodic array. (h)-(k) parts-per-billion level gas demonstration of the sensor. ((g)-(k) are reproduced from [104]).

A novel biosensor utilizing gold nanorods was developed by Wang et al. [105], harnessing the LSPR phenomenon. The biosensor was specifically designed for the detection of the hepatitis B surface antigen, which serves as an indicator of active viral replication in the hepatitis B virus. Recently, Sharifi et al. [102] designed an ultrasensitive LSPR biosensor using gold crystalline nanostructures to detect CA-19-9 protein in serum samples from pancreatic cancer patients (Fig. 7 (a)-(c)). Through meticulous optimization, the biosensor achieved an impressive detection limit of 0.0001 U/mL. In another study, Qiu et al. [103] employed functionalized gold nanoparticles coated with complementary DNA to validate the application of LSPR sensing in detecting oligonucleotides encoding specific sequences of the SARS-CoV-2 virus. They achieved this by integrating the LSPR technique with a thermoplasmonic effect, successfully attaining an exceptional sub-picomolar (sub-pM) detection limit (Fig. 7 (d)-(f)). In a recent study, Mid-IR ozone gas detection is reported by Ghanim et al., [106] in  $SiO_2$  film utilizing LSPR enhanced micrometer-sized antenna (Fig. 7 (g)-(k)). Improving sensitivity in LSPR sensors can be achieved by optimizing nanoparticle size and shape for enhanced plasmonic resonance, and by enhancing surface functionalization techniques to increase target molecule binding affinity [107].

### 3.3 Surface-Enhanced Raman Spectroscopy

Surface-Enhanced Raman Spectroscopy (SERS) is an advanced analytical method that amplifies the weak Raman scattering signal of molecules by exploiting their interaction with metallic nanostructures. Upon interaction with

these nanostructures, molecules undergo a process where the incident laser excitation triggers the emergence of localized surface plasmons, thereby inducing substantial amplification of the electromagnetic fields in the immediate vicinity of the nanostructures. Consequently, the Raman scattering signals emitted by the molecules undergo a pronounced enhancement, enabling their detection and characterization even at minute concentrations [108, 109].

The origins of SERS can be attributed to pioneering investigations conducted in the 1970s by Fleischmann, Hendra, and McQuillan [110] as well as Albrecht and Creighton [111], wherein they documented the observation of heightened Raman scattering signals from pyridine-adsorbed on uneven metal surfaces. Subsequently, substantial advancements have been achieved in comprehending the fundamental principles governing SERS and in the development of customized metallic nanostructures tailored to yield superior enhancement factors. Two primary mechanisms contribute to generating SERS enhancement: electromagnetic enhancement and charge transfer (also termed as chemical enhancement, which is a non-plasmonic condition) [112]. The electromagnetic enhancement can be viewed as an extreme scenario of surface-enhanced fluorescence (SEF), wherein the limited Raman scattering cross-section inhibits plasmon quenching. Consequently, the electric field magnitude during the Raman signal becomes insignificant. However, there is a localized field enhancement due to the excitation and emission of plasmons which is 108 times the normal Raman scattering, thus offering an overall enhancement [113, 114].

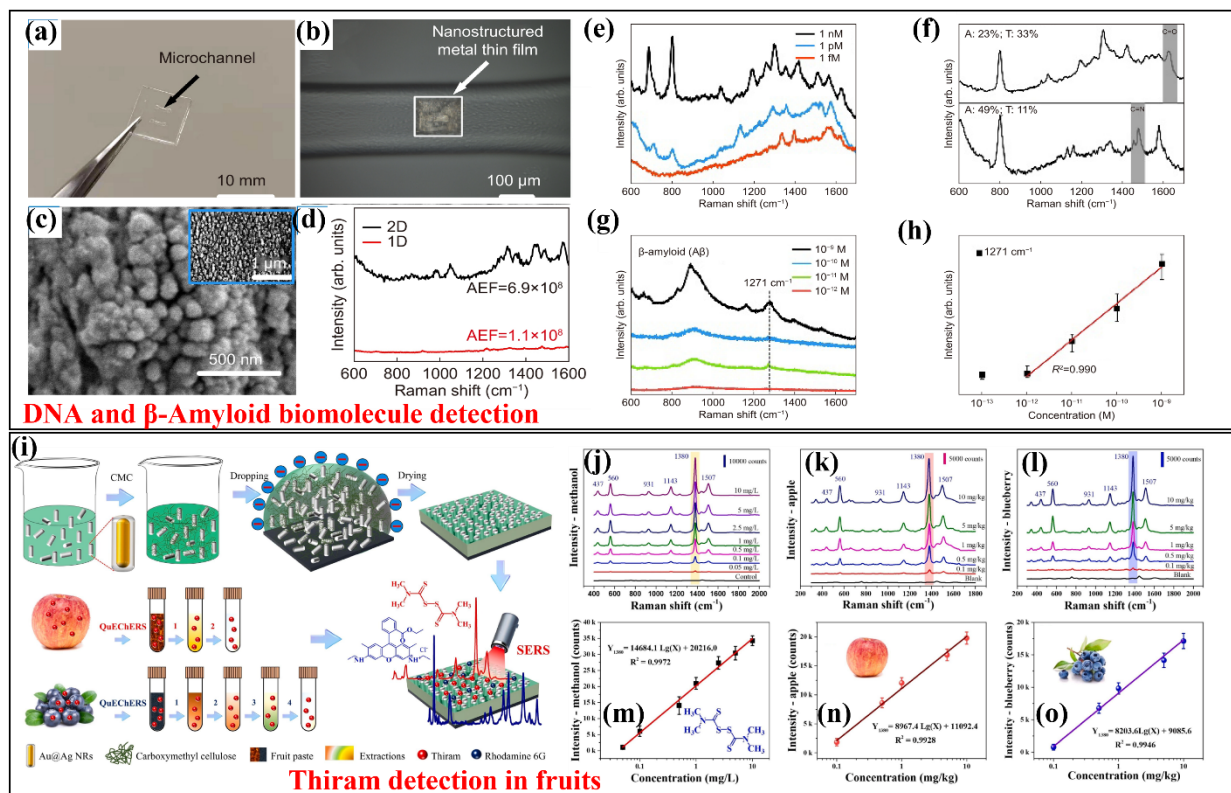


Figure 8 Microfluidic SERS chip created using hybrid fs laser processing. (b) SERS substrate within a glass microchannel. (c) Nanodots formed by secondary laser scanning. (d) Raman spectra of  $10^{-9}$  M Rhodamine 6G (R6G) on 2-D (black) and 1-D (red) nanostructured SERS substrates. (e) LI-SERS Raman spectra for DNA sequences at varying concentrations. (f) Raman spectra for 10 fM DNA sequences with different base ratios, highlighting peaks at  $1640\text{ cm}^{-1}$  (C=O) and  $1474\text{ cm}^{-1}$  (C=N). (g) Raman spectra of  $A\beta$  (29-40) at different concentrations using LI-SERS, (h) demonstrating a linear relationship of Raman intensity at  $1271\text{ cm}^{-1}$  with concentration (red line) [119]. (i)-(o) SERS spectra of thiram at different concentrations in methanol (j), apple (k), and blueberry (l) using the Au@Ag NRs-CMC chip; (m-o) Correlation between SERS intensities of thiram at  $1380\text{ cm}^{-1}$  and the logarithm of thiram concentration in methanol (m), apple (n), and blueberry (o), respectively [120].

Silver and gold nanomaterials have emerged as highly suitable options for enhancing the SERS signal and improving detection sensitivity. They provide rapid, efficient, cost-effective, and reliable SERS platforms for detecting minute quantities of biomolecules and pathogens, even at the single-cell level. This is attributed to their distinctive chemical, physical, and optical properties. Notably, core-shell structures like Au/Ag nanoparticles exhibit outstanding performance as SERS substrates due to significantly higher enhancement factors (EFs) [115–117]. Vancomycin-coated SERS enables rapid culture-free detection of bacteria in clinical samples, offering a 1,000-fold increase in capture without spectral interference. It selectively captured bacteria from human blood and shows potential for drug-resistance testing, advancing SERS-based biochips for clinical microorganism detection [118].

Bai et al. [119] presented a novel SERS platform called the liquid interface-assisted SERS (LI-SERS) method. It enables the label-free trace detection of biomolecules with detection limits ranging from pM to fM. The LI-SERS method demonstrated ultrahigh sensitivity and versatility in detecting deoxyribonucleic acid and  $\beta$ -Amyloid ( $A\beta$ ) in trace concentrations, featuring its unique capabilities for analytical applications (Fig. 8(a)-(h)). In another study, Hu et al., [120] engineered a high-performance, homogeneous SERS chip by integrating shell Au@Ag nanorods with carboxymethylcellulose hydrogel, achieving high sensitivity in trace-level pesticide residue detection. The study exhibited excellent performance in detecting thiram residues in fruits, including those with low and abundant pigment interferents like methanol, apples, and blueberries, with detection limits of 42, 58, and 78 ppb, respectively (Fig. 8(i)-(o)).

Various sensing methods discussed earlier offer distinct advantages and drawbacks. SPR/LSPR sensing stands out for its label-free nature and straightforward setup, but it is susceptible to environmental disturbances. SPR imaging, with its label-free approach and capacity for multi-channels, is advantageous; however, it grapples with channel crosstalk issues that limit resolution. On the other hand, SERS presents itself as a high-sensitivity option with selectivity for different biomarker species, albeit at the expense of requiring costly equipment. The integration of multiplex capabilities proves beneficial by reducing bioreaction durations and enhancing molecular binding, yet, it demands a complex system setup. Each method offers unique benefits while necessitating careful consideration of their respective limitations. Considering the significant significance and effectiveness of plasmonic-based biosensors in recent years, we have exemplified very few reports in Table 3, presenting a promising alternative platform in contrast to conventional sensing techniques.

*Table 3 State-of-the-art derived from diverse plasmonic-based biosensors.*

Sensing Method	Targeted Biomarker	Limit of Detection	Application
SPR	ErbB2	3.8 ng/ml	Breast Cancer Detection [121]
SPR	Tropomyosin	1 $\mu$ g/ml	Seafood Allergens Detection [122]
LSPR	Glypican-1	400 particles/ml	Pancreatic Cancer Detection [123]
LSPR	SARS-CoV-2	319 Copies/ml	COVID-19 Detection [124]
SERS	Shiga Toxin (Stx2)	0.49 aM (Enhancement Factor 1010)	Foodborne Pathogen Detection [125]
SERS	Bilirubin	10–9 M	Diagnosis of Jaundice [126]

## 4 Progressing Towards On-Chip Spectral Sensing

### 4.1 On-chip Absorption-based Sensing

On-chip absorption spectroscopy, also known as direct absorption spectroscopy (DAS), is an emerging technique that utilizes integrated photonic devices to conduct spectroscopic analysis directly on minute samples of materials within a microchip. This technology holds immense promise for various applications, ranging from chemical sensing and environmental monitoring to biomedical diagnostics. By miniaturizing the entire spectroscopy setup onto a chip, on-chip absorption spectroscopy offers significant

portability, cost-effectiveness, and scalability advantages, which is highly beneficial for field applications and point-of-care diagnostics, where real-time, on-site analysis is crucial.

In resemblance to the bulk spectroscopy method, on-chip absorption spectroscopy works on the Beer-Lambert law [127] as given in equation 2 below,

$$I = I_0 \exp^{-\alpha\gamma L} \quad (2)$$

In the given context,  $I_0$  represents the initial intensity of the incident light,  $\alpha$  denotes the absorption coefficient of the medium,  $L$  represents the interaction length, and  $\gamma$  is the medium-specific absorption factor, characterizing the impact of enhanced light-matter interaction due to dispersion. In traditional free-space systems,  $\gamma$  is equal to 1, necessitating a significant value of  $L$  to achieve sufficient sensitivity in measuring the intensity ratio  $I/I_0$ . However, in the case of on-chip systems, where  $L$  is significantly reduced, a high value of  $\gamma$  is important to compensate for this reduction in length. The on-chip system has the capability to tailor  $\gamma$  as per the perturbation theory [64, 128], as given in equation 3.

$$\gamma = f \frac{c \cdot n}{v_g} \quad (3)$$

where " $c$ " denotes the velocity of light in free space,  $v_g$  represents the group velocity in the medium with an effective index  $n$ , and  $f$  signifies the filling factor, indicating the relative fraction of the optical field present in the analyte medium. Consequently, by adjusting the group velocity and filling factor, it becomes possible to amplify the sensitivity of the engineered sensor.

Initially, researchers favored near-infrared (NIR) spectroscopy due to its advantages, such as reduced absorption by water and higher tissue penetration with readily accessible source and detector, making it suitable for various biomedical and analytical applications [128–131]. The multipass cell configuration is one of the common elements that has been extensively utilized to enhance the interaction of light with the analytes in the absorption-based spectroscopy method. Guo et al. [132] proposed a compact portable laser sensor using a multi-cell incorporated near-infrared laser absorption spectroscopy, selectively detecting trace ammonia ( $NH_3$ ) at  $1.51 \mu m$  and attaining a minimum detection limit of 0.16 ppm through Allan deviation analysis. Yet, achieving high sensitivity without employing a bulky and alignment-sensitive multipass gas cell to enhance interaction length is challenging when focusing on the portable sensing system. Relying solely on on-chip interaction (without multipass cell configurations), it is challenging to achieve satisfactory performance in key parameters like sensitivity and minimum detectable concentration. Fully on-chip absorption spectroscopy is demonstrated by Tombez et al. at a wavelength of  $1.65 \mu m$  for methane sensing using an evanescent coupling mechanism in the curly-designed optical waveguide. Their results showed detection limits below 100 ppm by volume [131]. However, hundreds of ppm-level detection is not enough for several practical applications. There is certainly a margin for scientific innovation to fill this gap. In this context, an engineered photonic waveguide holds great promise for substantially enhancing the interaction between light and analyte through improved light confinement, and/or with dispersion engineering, interaction time can be increased without enlarging the physical waveguide dimensions. Based on the dispersion-engineered on-chip photonic structure, our group has demonstrated a  $300 \mu m$ -long Si photonic crystal slot defect waveguide NIR absorption spectrometry at around  $\lambda = 1.69 \mu m$  for the detection of xylene in water and reported concentrations up to 0.1 ppm (0.086 mg/l) [130].

To follow further advancement in the absorption spectroscopy technique, the mid-infrared (MIR) regime (wavelengths from 2 to  $20 \mu m$ ) has proven to be a turning factor for the on-chip spectrometer. MIR offers enhanced molecular specificity as it corresponds to fundamental vibrational modes often referred to as the

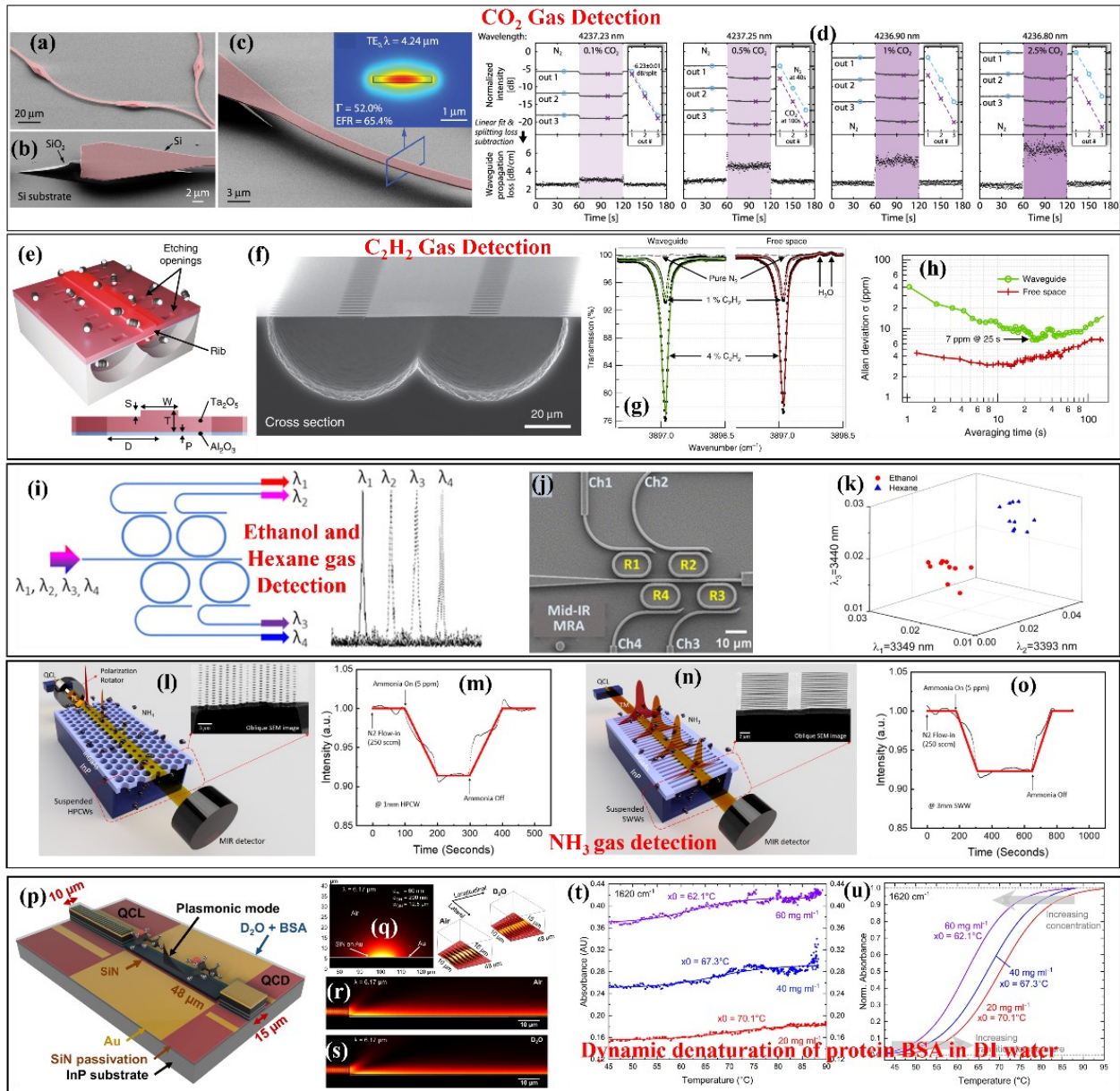


Figure 9 Recent advancements in on-chip absorption spectrometer. (a)-(c) SEM image of suspended silicon waveguide operating at  $\lambda = 4.2\mu\text{m}$ , inset shows the simulated TE polarized mode profile. (d) gas absorption characteristics with 0.1%, 0.4%, 1% and 2.5% CO<sub>2</sub> concentrations (top panel) and respective propagation loss (bottom panel) [134] (e) Shallow rib tantalum pentoxide membrane core (Ta<sub>2</sub>O<sub>5</sub>), bottom-passivated with Al<sub>2</sub>O<sub>3</sub> designed to support TM optical mode. (f) SEM of fabricated device. (g) Measured spectra using a 2cm long waveguide (left) and in free space equivalent pathlength (right) at various C<sub>2</sub>H<sub>2</sub> concentrations in N<sub>2</sub>. (h) Allan deviation plot corresponding to the concentration data time series for 1% C<sub>2</sub>H<sub>2</sub> [141]. (i) Depiction of four-channel MRR operating at distinct wavelengths. (j) SEM image. (k) 3D absorption plot of hexane (blue) and ethanol (red) [147]. (l) diagram depicts a suspended hollow photonic crystal waveguide and cross-section image in the inset. (m) Ammonia detection at 5 ppm with TE polarized propagating mode. (n) illustration of suspended sub-wavelength grating-based waveguide and SEM image (inset). (o) Ammonia detection at 5 ppm with TM polarized propagating mode. [148] (p) Pictorial view of monolithic integration of QCL/QCD with the plasmonic waveguide. (q)-(s) Simulated plasmonic mode in the waveguide. (t) Denaturation measurement of BSA at different concentrations. (u) Evaluation of Boltzmann-fit curves illustrates the temperature- and concentration-dependent characteristics of the sigmoidal-shaped absorbance curve. [149].



enables the accurate identification of the majority of chemical molecules that undergo alterations in their dipole moment during these vibrational modes. For on-chip spectrometers, exploiting silicon's optical transparency from 1.1  $\mu\text{m}$  to 8  $\mu\text{m}$ , the majority of photonic sensing waveguides are constructed in silicon-on-insulator (SOI). These waveguides are frequently preferred due to their compatibility with Complementary Metal-Oxide-Semiconductor (CMOS) technology. Additionally, they provide high index contrast, facilitating the core-cladding waveguiding phenomenon. However, the transparency of the SOI-based platform is confined up to 3.7  $\mu\text{m}$  due to the presence of oxide cladding. An alternative approach involves using free-standing silicon membranes, enabling the utilization of the entire low-loss silicon spectrum [134, 135]. In one such approach, Briano et al. illustrated the detection of  $\text{CO}_2$  gas at a 4.2  $\mu\text{m}$  wavelength utilizing an integrated silicon waveguide, with a  $\text{CO}_2$  sensitivity reaching 44% of that achieved in free-space sensing (Fig. 9 (a)-(d)). However, the fabrication of such suspended structures is challenging, giving rise to concern regarding their durability. Our group engaged in this effort has conceptualized an exclusive vertical photonic crystal waveguide entirely made of silicon. By leveraging the photonic bandgap, slow-light within the air core defect enables simultaneous multiplex sensing in a single shot using affordable mid-IR LEDs [136–138]. Researchers are also exploring other promising material platforms like  $\text{Si}_3\text{N}_4$  and silicon on sapphire (SoS) [139, 140] to avail high contrast core-clad choice with an extended low-loss window in the Mid-IR regime. Parallely, several advanced materials are also being utilized for this purpose [141, 142]. For example, Vlk et al. presented an integrated waveguide sensor for mid-infrared (MIR) spectroscopy with a notable 107% evanescent field confinement in the air. Experimental validation at 2.566  $\mu\text{m}$  demonstrated a remarkable detection limit of 7 ppm for acetylene, utilizing a 2cm long  $\text{Ta}_2\text{O}_5$  waveguide [141] (Fig. 9 (e)-(h)). Various methods have been proven beneficial to improve light-analyte interaction by improving optical confinement in the cladding/sensing region (f) through structure optimization [134, 143–146]. In another absorption spectroscopy approach, Zhou et al. employed a micro-ring resonator array (MRA) for multiwavelength mid-IR sensing, guiding light from a broad source into specific channels on compact spectrometers. Using small micro-rings on silicon-rich silicon nitride films, the system achieves a sizable free spectral range (FSR) of 100 nm across four channels and selectively detects hexane and ethanol vapor pulses at their mid-IR absorption bands (Fig. 9 (i)-(k)) [147].

The seamless integration of light sources with photodetectors and low-loss optical sensing waveguides is consistently preferred, offering an on-chip spectrometer that is insensitive to alignment variations and resilient to vibrations. Undoubtedly, the selection of materials plays a crucial role in such integration. Currently, the most effective operations of quantum cascade lasers (QCLs) have been demonstrated on the InP platform. The well-matched lattice constant of  $\text{In}_{0.53}\text{Ga}_{0.47}\text{As}$  with InP materials exhibits optically transparent characteristics across a broad-spectrum range ( $\lambda \approx 3 \mu\text{m}$  to 15  $\mu\text{m}$ ) [150]. Notably, the InGaAs/InP platform stands out as the optimal choice, allowing for the epitaxial growth of QCL/QCDs on the same wafer without needing costly wafer/chip bonding processes. Numerous attempts have been undertaken to realize a spectrometer with monolithic integration on the InP-based platform, as evident in works such as [64, 149, 151, 152]. In the direction to achieve a monolithic spectrometer, our group has experimentally detected 5 ppm ammonia using a 1 mm suspended holey photonic crystal waveguide and a 3 mm suspended subwavelength grating cladding waveguide in InP/InGaAs platform. Additionally, we estimate a minimum detectable gas concentration of 84 ppb based on the Beer–Lambert infrared absorption law [148] (Fig. 9 (l)-(o)). Recently, Hinkov et al. [149] introduced a compact chip-scale sensor utilizing quantum cascade technology for real-time monitoring of molecular dynamics in liquid solutions. Their fingertip-sized device integrates emitter, sensing, and detector functions on a single chip. They demonstrated excellent performance high absorbance (55 times more than bulky) and wide concentration coverage (75  $\mu\text{g}\cdot\text{ml}^{-1}$  to 0.092  $\text{g}\cdot\text{ml}^{-1}$ ) (Fig. 9 p-u). Nevertheless, it's important to highlight that a

drawback of employing such a monolithic approach is that if any individual component malfunctions or if the sensing waveguide becomes contaminated, particularly common in liquid-type analyte sensing scenarios, the entire chip must be discarded. This aspect holds significant importance when considering cost estimation.

## 4.2 On-chip Fourier Transform Spectrometers

Fourier Transform Spectroscopy (FTS) is a versatile technique capable of analyzing a broad range of materials, including solids, liquids, and gases. The principle of FTS involves generating a spectrum by applying a Fourier Transform to a time-domain interferogram produced by an interferometer, such as the Michelson interferometer (MI) or lamellar grating interferometer. Compared to dispersive optical spectrometers, FTS offers advantages such as multiplexing, high optical throughput, high resolution, and a high signal-to-noise ratio (SNR). However, conventional free-space optic FTSs are bulky and expensive, limiting their applicability in various fields such as remote sensing, airspace exploration, environmental monitoring, meteorological monitoring, biomedical science, and nanotechnology. In response, there is a growing demand for miniaturized on-chip FTSs driven by the need for high sensitivity, cost-effectiveness, non-invasiveness, and real-time detection capabilities, particularly for sensing applications. Integrating FTS components onto microchips presents challenges, especially in implementing MI configurations with moving parts, due to limited component travel ranges. Nonetheless, the miniaturization of FTS onto on-chip platforms promises a transformative shift in analytical capabilities, enabling the development of compact, portable devices that enhance accessibility and reduce costs. Moreover, integrating FTS components on chips for sensing applications improves portability and paves the way for integration with other on-chip technologies. This advancement holds promise for creating highly integrated, efficient analytical sensing systems for diverse applications. This section explores recent advances, challenges, and applications of on-chip FTS, emphasizing the development of efficient and adaptable analytical tools.

The successful integration of microelectromechanical systems (MEMS) technology into FTSs has significantly progressed toward on-chip FTS devices [153]. MEMS mirrors have replaced the bulky scanning modules of traditional MI-based FTSs, leading to emergence of various MEMS-based FTS devices with different actuation mechanisms. With a special emphasis on the integration of MEMS technology aiming at miniaturization, portability, and improved spectral resolutions, researchers have explored various MEMS-based micromirror designs, including comb-based In-plane electrostatic technique [154, 155], MEMS micromirror with out-of-plane electrostatic capabilities [154, 156] and lamellar grating actuators [154, 157, 158], demonstrating high performance and portability. remarkable performance and portability. In FTS, the two main performance parameters are achieving a broad spectral range and fine spectral resolution. To address these challenges in chip-scale optical spectrometers, Fathy et al., [159], utilized parallel FTIR with multiple interferometers in a MEMS-based infrared spectrometer on a silicon chip. They successfully demonstrated effective monitoring and exhibited distinct methane absorption bands in greenhouse gas analysis. However, the complexity and challenges of fabrication increase when multiple interferometers are involved (Fig. 10 (a-d)). Qiao et al. presents a method involving a MEMS-based on-chip computational spectrometer designed for mid-infrared sensing in the range of 3.7–4.05  $\mu\text{m}$ . By leveraging time-domain modulation of reconfigurable waveguide couplers, their approach presents advantages such as low power consumption, single-pixel detection, and multiplexing capabilities. The research showcases the analysis of a broad absorption spectrum of nitrous oxide gas, achieving a resolution of 3 nm. (Fig. 10 (e-k)) [160].

MEMS-based on-chip FTS systems offer advantages but face challenges such as limited mirror range, susceptibility to environmental conditions, complex fabrication, durability concerns, scaling issues,

alignment requirements, and optical trade-offs. These factors impact their spectral resolution, performance, and long-term reliability. In an alternative approach, researchers have explored static FTSs on a chip, which involve a static approach or electro-optic/thermo-optic-based tuning of the optical signal via changing waveguide refractive index. These approaches avoid moving parts (referred to as static FTSs on chip), such as stationary-wave integrated FTS (SWIFTS) and spatial heterodyne Fourier Transform spectrometers (SHFTS). SWIFTS approach involves creating a fixed wave pattern through the interference of either opposing or parallel-propagating waves [161–163]. Coarer et al. [162] utilized

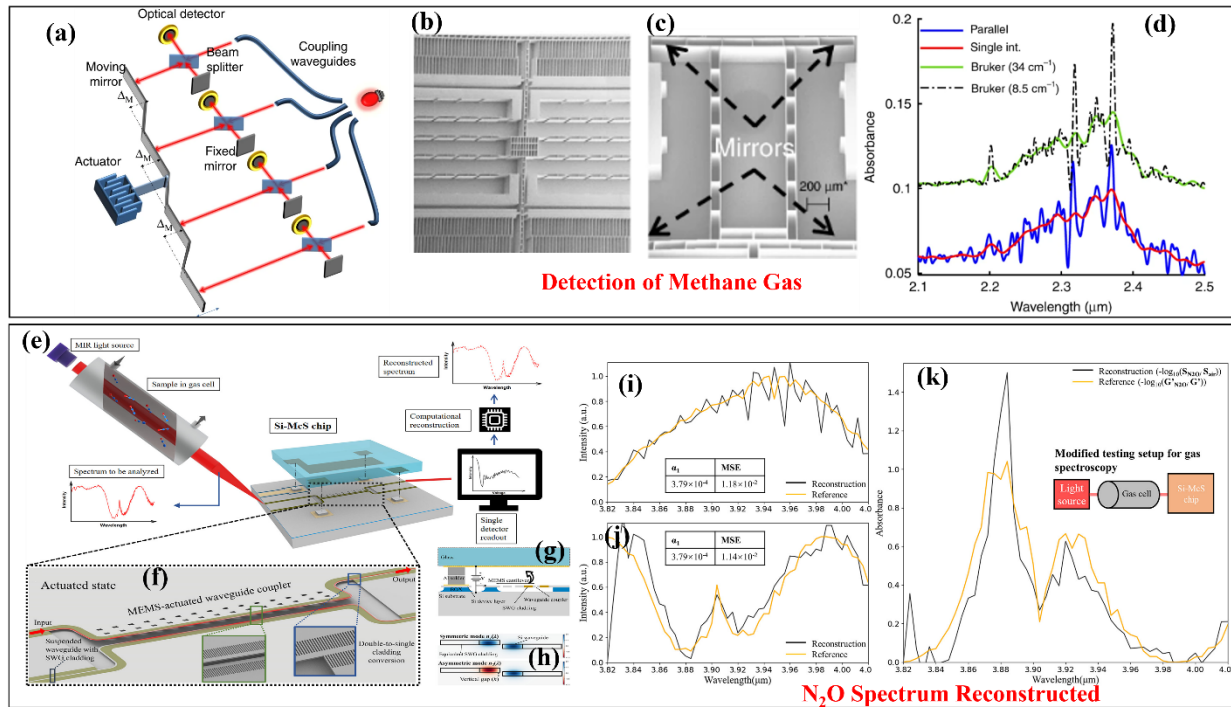


Figure 10 MEMS-based on-chip FTSs. (a) Illustration of parallel interferometers sharing a common actuator, featuring spatially shifted moving mirrors to acquire shifted interferograms. (b) SEM image displaying the actuator. (c) SEM image depicting the moving mirror arm. (d) Comparative analysis of methane absorbance curves measured by parallel interferometers (blue) and a single interferometer (red), contrasted with absorbance from a benchtop spectrometer for corresponding resolutions [159]. (e) MIR spectroscopy system employing the Si-McS chip: MIR light traverses the gas cell, and the absorbed light is analyzed on the Si-McS chip through computational reconstruction based on the measured interferogram. (f) Close-up of the spectrometer with actuation element, showing upward movement of the MEMS cantilever. (g) Cross-section view illustrating applied bias and relative motion during operation. (h) Field distribution of propagating mode profiles of the coupler. (i) and (j) Reconstruction of the spectrum for air and N<sub>2</sub>O gas respectively. (k) Calculated absorbance unveils spectral features indicative of detected N<sub>2</sub>O gas. [160].

SWIFTS for the first time to develop a highly compact one-dimensional integrated spectrometer, demonstrating a resolution of 4 nm and a bandwidth of 96 nm using a single stationary MZ, resulting in a compact device. However, this type of FTS device has a limitation of narrow bandwidth due to the limited optical path delay (OPD) and pitch distance of the detectors for detecting standing waves. In contrast, SHFTS achieves high resolution through an array of stationary MZIs with a linearly increasing optical path delay or difference. A fixed propagation phase delay is achieved through a combination of multiple elements providing stepwise phase shifts and/or by thermally or electrooptically modifying the effective refractive index of the waveguide to achieve the desired phase shift. Our group has demonstrated several on-chip FTS devices on a variety of material platforms including SoS, Si, and SiN<sub>x</sub>. In one such endeavor,

Heidari et al. [164] demonstrated an on-chip FTS on silicon-on-sapphire, featuring twelve MZIs with a linearly increasing OPD. The strip waveguides exhibited a propagation loss of  $5.2 \text{ dB}\cdot\text{cm}^{-1}$ , and successful optical spectrum retrieval from an inter-band cascade laser at  $3.3 \mu\text{m}$  demonstrated a resolution better than  $10 \text{ cm}^{-1}$ .

It is widely recognized that the spectral resolution and bandwidth of SHFTS rely on the quantity of MZIs and maximum OPDs. Striking a balance is imperative to accommodate the constraints of limited chip-scale and detection conditions. To achieve unprecedented resolutions, various designs of static on-chip FTS based on planar waveguide unbalanced MZI arrays have been investigated [165]. Achieving fine resolution with broad operation necessitates an impractically large number of MZI arrays, significantly

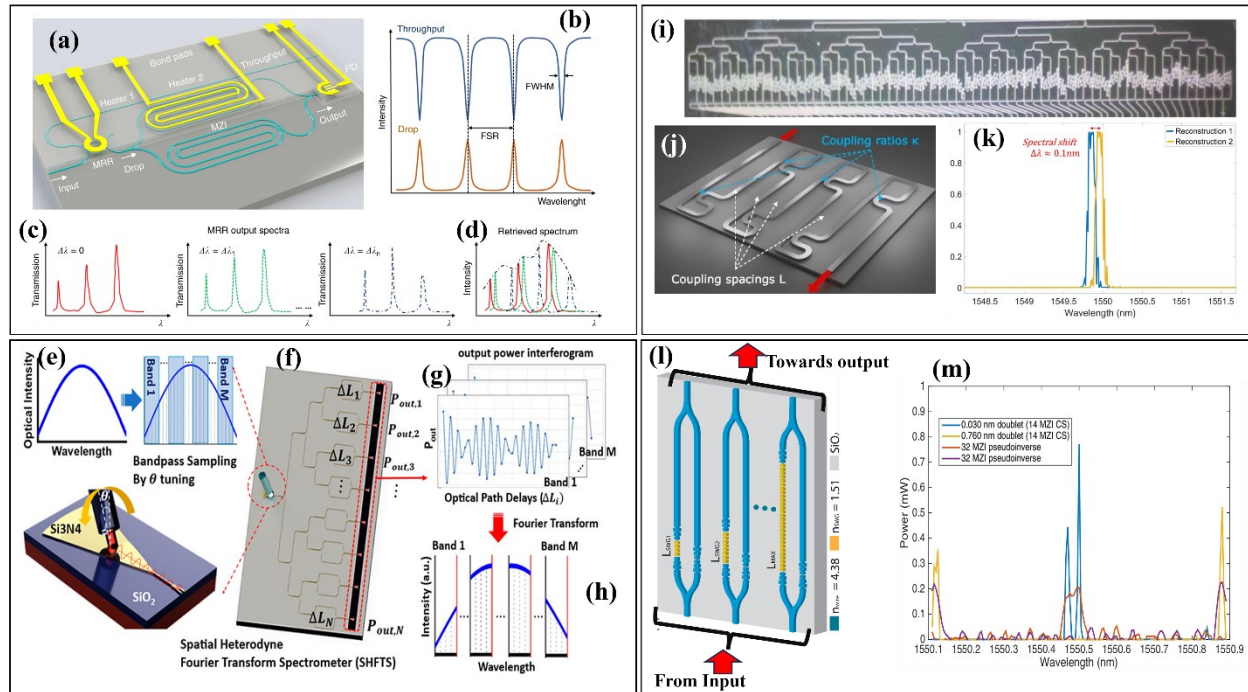


Figure 11 Various on-chip Fourier transform spectroscopy methods are illustrated: (a) RAFT spectrometer with an MRR and MZI integrated with a PD, (b) MRR transmission spectra, (c) Output filtered spectra from the MRR, (d) Retrieved spectra from the tunable MZI, (e) SWGC operation as a coupler and tunable-bandpass filter, (f)  $\text{Si}_3\text{N}_4$  SHFTS chip with  $N$ -MZIs, (g) Spatial interferograms from MZI array output powers, (h) Reconstructed narrow-band spectra by Fourier transform, (i) Microscopic images of the spectrometer, (j) One of the 64 filters, (k) Application for fiber Bragg grating sensor, (l) Light directed to an array of interferometers, and (m) Spectra retrieval using unapodized interferometric measurements from a subset of MZIs.

increasing the device footprint. For instance, a standard SHFTS device demonstrated earlier featured a 24 MZI array, offering a 5 nm resolution and a 60 nm bandwidth centered at  $\lambda_0 = 900 \text{ nm}$  on the  $\text{Si}_3\text{N}_4$  platform [164]. In another example, Zheng et al. [166] demonstrated a micro-ring resonator-enhanced FTS. This innovative device incorporates a tunable MZI linked with a tunable MRR to significantly improve resolution. Notably, the MRR elevates the resolution to an impressive 0.47 nm, surpassing the Rayleigh criterion for tunable MZI-based FTS (Fig. 11(a)-(d)). In another innovative approach to overcome the mentioned trade-off between bandwidth and resolution, Min et al. [167] reported broadband optical spectrometers utilizing a subwavelength grating coupler integrated with the SHFTS based on an unbalanced MZI array. To overcome the trade-off, their proposed approach uses bandpass sampling to reconstruct narrow-band channels and achieves a broad-spectrum coverage of 400 nm (650-1050 nm)

with a 2-5 nm resolution (Fig. 11(e)-(h)). Li et al. [168] address the bandwidth-resolution trade-off effectively through an innovative computational spectrometer. Unlike conventional resonator-based approaches, they employ a unique type of broadband filter known as multi-point self-coupled waveguide (MPSCW). By leveraging the low-linear dependency among 64 filters, they successfully attain a broad bandwidth of 100 nm while maintaining a high resolution of 0.1 nm (Fig. 11(i)-(k)).

Continuing with advancements in digital spectrometry, Kita et al. have demonstrated a high-resolution and scalable on-chip digital FTS, proposing digital signal processing techniques and optical switches to dynamically select discrete OPDs, enabling precise spectral analysis [169]. In another approach, Miguel et al. [161] have demonstrated an alternative on-chip SHFTS approach that utilizes spatial heterodyning and optical path tuning via the thermo-optic effect. This approach effectively overcomes the bandwidth-resolution tradeoffs encountered in conventional devices. The method involves an array of MZIs with cumulative optical path length differences and mutual thermal tuned lengths. The output interferogram captures data for various temperatures, enabling fine resolution and broad operation without the necessity for large interferometers. The mid-IR spectrometer utilizing Ge-rich SiGe waveguides achieves a four-fold increase in bandwidth ( $603 \text{ cm}^{-1}$ ), consequently attaining high resolution ( $< 15 \text{ cm}^{-1}$ ). Hugh Podmore et al. [170] demonstrated slow-light induced OPD using an MZI-based FTS on a photonic chip using spatial heterodyne configuration and a compressive-sensing technique. In this design, the MZI arms are designed to have a group index difference through the required phase delay by controlling the length of the subwavelength region in the delayed arm. Then, the compressive-sensing exploits spatial interferogram sparsity or compressibility (down-sampling) of the spatial interferogram, enabling accurate reconstruction of input spectra with full resolution and bandwidth using only 14 MZIs (Fig. 10 (i)-(j)). In order to perform sensing analysis utilizing an FTS device, Yoo et al. [171, 172] integrated MRR and on-chip FTS to eliminate the need for an external optical spectrum analyzer. The output resonance peaks reconstructed through the integrated SHFTS, provide a spectral resolution of approximately 3.1 nm and a bandwidth of about 50 nm and achieve a remarkable limit of detection of 0.042 RIU. The integration of these components on a single SOI wafer streamlines the sensing process while enhancing the overall performance and sensitivity of the biosensor system.

### 4.3 Wavelength Modulation Spectroscopy

Wavelength Modulation Spectroscopy (WMS) has emerged as a powerful and versatile spectroscopic analysis technique, offering notable advancements over conventional methods such as direct absorption spectroscopy. This section provides an overview of the WMS principle, advantages, and applications, with a particular focus on recent developments in higher harmonic detection and its integration into photonic on-chip systems. The WMS technique enhances detection signal-to-noise ratios by modulating the laser frequency (or wavelength) at a specific frequency (or wavelength) and amplitude, enabling precise spectral analysis and selective detection of molecular species of interest. The sinusoidal modulation improves the SNR of measurements by reducing low noise ( $1/f$ ) contributions [173–175]. The laser frequency ( $\nu(t)$ ) is modulated at a particular frequency,  $f_m$  (in kHz), and a modulation amplitude  $V_m$ ; then the modulated laser frequency has the mathematical form as [176, 177]:

$$\nu(t) = \nu_c + V_m \cos(2\pi f_m t) \quad (4)$$

Where  $\nu_c$  is the laser center frequency. The modulated laser beam traverses through the sample, inducing variations and changes in transmitted light intensity at the modulation frequency ( $f_m$ ). Unlike the conventional approach, where the transmittance,  $T = I(\nu) / I_0$  is measured, WMS technique quantifies

relative absorption,  $\bar{A}$  in terms of the incident intensity ( $I_0$ ) and the intensity of light after transmitting through the absorption medium ( $I$ ), which is defined as [176, 177]:

$$\bar{A} = \frac{\Delta I}{I_0} = \frac{I_0 - I}{I_0} \quad (5)$$

A photodetector records these modulated intensity fluctuations, and its output, containing both amplitude and phase modulation, undergoes analysis in a phase-sensitive device, typically known as a lock-in-amplifier. This process extracts higher-order harmonics ( $Nf_m$ ) of the modulation frequency (where  $N = 1, 2, 3$ , etc.). For instance,  $2f_m$  is the second harmonic and  $3f_m$  is the third harmonic, and so forth. Analyzing these higher harmonic terms within a Taylor or Fourier series contributes to a more accurate representation of the signal to be detected. Including higher harmonics enables the capture of distinct absorption line profiles, which is particularly beneficial for overlapped and complex absorption line features.

In the literature, various theoretical frameworks for the WMS technique have been proposed [178 – 182]. Initial studies explored employing a Taylor expansion of the spectral profile of the absorption to derive higher harmonics of the modulated absorption signal from the absorption line's  $N^{\text{th}}$  derivative. This method proved effective when peak intensity of the modulated signal was significantly smaller than the half-width ( $\Delta\nu_p$ ) of the absorption profile (i.e.,  $V_m \ll \Delta\nu_p$ ) [181– 183]. However, when using the WMS technique, the Taylor expansion approach becomes invalid when modulation amplitudes exceed the width of the absorption profiles. Wilson utilized numerical integration [178] to handle modulation amplitudes of any magnitude [178], successfully solving the first three harmonics ( $1f_m, 2f_m, 3f_m$ ) for both Gaussian- and Lorentzian-broadened lines. Conversely, Arndt [179] presented an analytical solution grounded in Fourier analysis for all  $N f_m$  harmonics of a Lorentzian-broadened profile, although explicit expressions were provided only for the  $1f_m$  and  $2f_m$  components. The first experimental validations of these theoretical frameworks, employing diode lasers, were carried out by Reid and Labrie [181]. Additionally, calculations for the  $2f$  component of a Voigt profile are conducted, using the same numerical integration method as Wilson. Following progression in higher-order harmonics detection of modulation frequency ( $1f_m, 2f_m, 3f_m$ ), several demonstrations were carried out [184–187]. This technique offers enhanced sensitivity, selective detection of different molecular species, improved SNR, and the ability to reveal nonlinear effects in light-matter interactions. Therefore, higher harmonic detection finds applications in atmospheric science, trace gas analysis, and materials characterization.

WMS offers several advantages that contribute to its widespread adoption in various environmental, biomedical, and industrial applications. Its high sensitivity makes it well-suited for accurate measurements of low concentrations in trace gas analysis by the use of semiconductor lasers in the mid-infrared and near-infrared [173–175, 180, 188–197]. The selectivity of target analyte species is enhanced by focusing on specific wavelengths corresponding to the sample's absorption features. Additionally, interference can be reduced by choosing an appropriate modulation frequency, and background signals ( $1/f$  noise) can be effectively suppressed, leading to an improved SNR of the system. The quantitative nature of WMS analysis, correlating signal characteristics with species concentration, further establishes its utility and applicability in many trace gas sensing applications at high pressure and temperature. The versatility of WMS is reflected in its applications across diverse fields. Environmental monitoring [196 – 199], industrial process control [200–204, 204], and gas sensing benefit from the higher sensitivity and selectivity of the WMS technique. The technique is extensively used in studies related to atmospheric chemistry, air quality monitoring, and remote sensing applications. Its capability to detect trace gases in various matrices underscores its significance in medical applications such as human breath analyzers for lung cancer detection [205–207].

Recent advancements in WMS have extended its capabilities to chip-scale implementations. Studies, such as that by Mingquan Pi et al. [208, 209], explore the effectiveness of WMS in waveguide sensors compared to DAS. In "Methane Gas Detection Using Second Harmonic Signal" by Mingquan Pi, the study explores the use of WMS in waveguide sensors, demonstrating significant sensitivity improvements over direct absorption spectroscopy (DAS). The research focuses on optimizing mid-infrared waveguide methane sensors and fabricating ChG-on-MgF<sub>2</sub> sensors, achieving a 24x reduction in the limit of detection (LoD) compared to previous DAS-based sensors (Fig. 12 (a-d)) [208]. Recently, Zhao et al. [210] presented a novel on-chip acetylene (C<sub>2</sub>H<sub>2</sub>) sensor using SU8 polymer spiral waveguides. The sensor utilizes WMS and incorporates a Euler-S bend design, reducing sensor size by over 50%. Experimental validation shows a LOD down to hundreds of ppm, highlighting SU8's promise for compact, high-sensitivity on-chip gas sensing. We envision that WMS continues to evolve, driven by advancements in higher harmonic detection and on-chip implementation (Fig. 12 (e-h)). The sensitivity, selectivity, and noise reduction capabilities of WMS establish it as an asset across various sensing applications in scientific and industrial fields. With ongoing research and technological advancements, WMS technique integrating with on-chip components is likely to further expand its applications, addressing complex challenges in gas sensing and spectroscopic measurements.

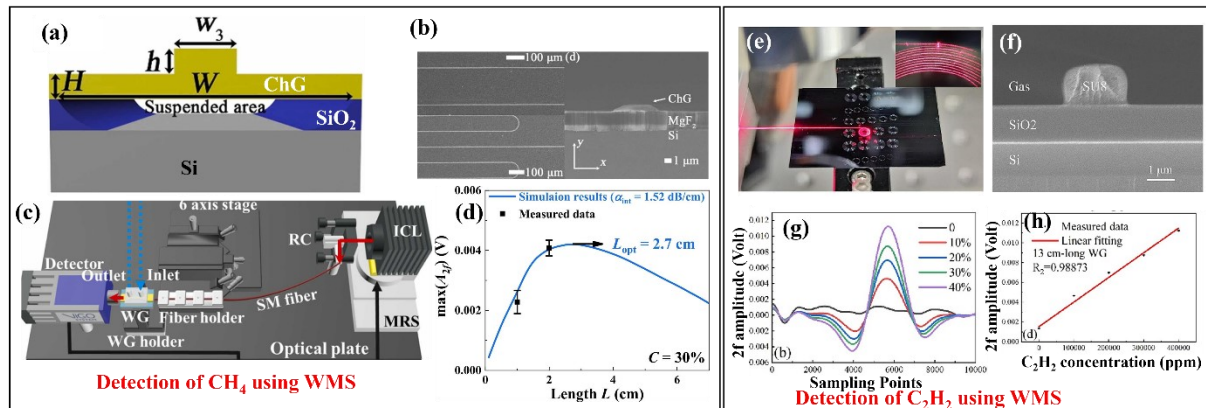


Figure 12 Experimental validation of WMS on a chip scale: (a) and (b) depict the schematic of a suspended optical waveguide made of chalcogenide material on top of a Si platform and SEM image respectively. (c) shows the schematic of the measurement system. (d) depicts simulation curve of  $\max(A_{2f})$  versus  $L$  and the measured  $\max(A_{2f})$  with  $L = 10$  mm and  $L = 20$  mm. (e)-(h) shows the WMS-based C<sub>2</sub>H<sub>2</sub> sensor where (e) shows microscopic photos with red light coupled into the spiral waveguide, (f) shows the cross-section electron-microscopic image of the SU8 waveguide on the silicon platform. (g) and (h) show the measured  $2f$  signal under various C<sub>2</sub>H<sub>2</sub> concentration levels and linear fitting curve for 13 cm-long waveguides.

#### 4.4 Photonic Frequency Comb Spectroscopy: Toward On-Chip Integration

An Optical Frequency Comb (OFC) is a spectrum consisting of discrete and equidistant spectral lines. OFCs play a crucial role in bridging the optical and radio or microwave frequency domains through a process known as frequency synthesis. This process involves linking the stability and precision of an optical frequency comb to a well-established and easily measurable radio or microwave frequency reference. OFCs have quickly become attractive in various applications, including precision frequency measurements, timekeeping, telecommunication, broadband molecular spectroscopy, gas sensing, and quantum information processing. Early methods for generating frequency combs [211, 212] are based on intra-cavity phase modulation. Later, mode-locked lasers with stabilized repetition rates and carrier-envelope phases became a common approach [213–215].

A commonly used mechanism generating evenly spaced spectral lines in a mode-locked laser is mathematically described by the comb equation  $f_n = f_0 + n \cdot f_r$ , where  $n$  is an integer,  $f_r$  is the comb tooth spacing (equal to the mode-locked laser's repetition rate or alternatively, the modulation frequency), and  $f_0$  is the carrier offset frequency, which is less than or equal to  $f_r$  ( $f_0 \leq f_r$ ). The comb equation emphasizes that only two parameters - the repetition frequency and laser offset frequency - are required to define each individual optical mode,  $f_n$ . The laser repetition rate,  $f_r$ , which is the inverse of the pulse-to-pulse timing  $\tau_r$ , is constant across the spectrum due to the cavity resonance modes from the mode-locking mechanism, ensuring the equidistant spectral lines of the OFCs [216]. Measuring  $f_r$  is straightforward and can be done using a photodiode and an RF spectrum analyzer to measure it directly.

Measuring  $f_0$  experimentally is challenging due to its connection to the optical carrier phase. In 1999, a method was proposed to generate a heterodyne beat at  $f_0$  through nonlinear self-referencing between the endpoints of the optical comb spectrum [217, 218]. The simplest implementation of heterodyning at  $f_0$  involves doubling the frequency of light from a low-end comb mode and then interfering it with fundamental light at twice that frequency to determine  $f_0$ , such that  $f_0 = 2 \cdot (n \cdot f_r + f_0) - (2 \cdot n \cdot f_r - f_0)$ . Implementing the mathematical concept of an optical frequency comb requires covering an optical octave of bandwidth, which is challenging due to the broadest mode-locked lasers typically being less than 100 nm.

In the 1990s, the development of highly engineered low-dispersion optical fibers enabled the generation of a coherent white light continuum using ultra-short laser pulses. This breakthrough, combined with optical frequency combs (OFCs) from Ti:sapphire lasers, led to rapid advancements in precision metrology. Within a few years later, various applications were demonstrated [212, 213, 219–224], including atomic clocks, optical frequency measurements, attosecond control, and direct molecular spectroscopy, marking a period of intense progress in the OFC research field. Stabilizing frequency combs involves employing various techniques, including phase-locking to external references such as GPS-disciplined oscillators [225], fiber stretching [226], feedforward and feedback control [227] (Kärtner et al., 2003), and the use of optical cavity resonators [228]. Additionally, carrier-envelope offset (CEO) stabilization using f-2f interferometers [213] and temperature control of critical components contribute to long-term stability in frequency comb systems [229].

After realizing how to stabilize OFCs, advancements in mode-locked laser (MLL) systems led to the evolution of solid-state and fiber-based optical frequency combs (OFCs). Diode-pumped solid-state and fiber lasers, particularly Er: fiber OFCs, dominated commercial success, providing near-continuous spectroscopic coverage from 400 nm to  $\sim 4 \mu\text{m}$ . The state-of-the-art MLL sources have transitioned from Ti:Sapphire laser systems to compact, environmentally stable Er: fiber OFCs, culminating in sub-100 fs Er/Yb:glass lasers that are highly compact and portable. Instead of using mode-locked lasers, non-linearity in photonics resonators can generate a frequency comb. A key advantage and prospect of this approach is that by using optical resonators, we can operate at high repetition rates ( $> 10$  GHz), which unlocks applications, and photonics integration is possible.

Optical microcavities enable new research fields to blossom, particularly in frequency metrology. The concept of microcavities originated in the 1990s [230], confining light in very small volumes for an extended amount of time. The traditional challenge is fabricating devices with very high-quality factors (Q factor). Braginsky and Ilchenko observed ultrahigh-quality factors inside glass microspheres, triggering research in the area of high-Q microcavities [231]. Confining light in a small volume for an extended time involves nonlinear optics as a key process. For example, second and third-order nonlinear optics effects are the driving forces for supercontinuum generation and Kerr-comb generation for frequency metrology [232]. Vahala et al. reviewed four different optical microcavities based on their light



confinement methods and discussed their diverse future applications [233]. One interaction worth noting is the optomechanical coupling that naturally occurs in optical microcavities due to the coupling between optical and mechanical modes. It has been of broad interest for a long time in the microcavity research field [234–236]. Another interaction inside micro-resonators is Kerr non-linearity, a well-known underlying process responsible for self-phase modulation and supercontinuum generation. In the context of micro-resonators, the nonlinear Kerr process allows an optical frequency comb to be generated, providing a framework to generate a very compact chip-scale frequency comb that can make frequency metrology and other applications ubiquitous [237].

Therefore, on-chip optical micro-resonators have become vehicles for these research fields, including quantum optical phenomena resulting from the coupling of light and mechanical motion in addition to the optical degree of freedom explored in the optical microcavity. Or they can be used to generate a frequency comb. The process underlying the optical generation is parametric oscillations, four-wave mixing where two pump photons are annihilated to generate a single idler photon. According to energy conservation, the excess of the idler photon needs to be compensated by reducing the signal frequency, thereby creating two equidistant sidebands. This process, opposite to conventional lasers, scales with  $1/Q^2$ .

Over the past fifteen years, there have been notable developments in the field of tiny and chip-scale optical frequency comb (OFC) sources. Semiconductor lasers have become highly versatile platforms with a broad wavelength range and the ability to be mass-manufactured at a reasonable cost. Examples of these lasers are mode-locked integrated external-cavity surface-emitting lasers (MIXSELs) and QCLs. In particular, MIXSELs exhibit sub-100 fs pulse production and, when optically pumped, over 1 W of optical power. Micro-resonator systems, known as micro-combs, operate as low-loss optical resonators, showing promise for chip-scale integration. Despite challenges in efficient soliton formation, micro-combs have achieved coherent detection of  $f_0$  and expanding to an optical octave at mode spacing (<30 GHz). However, thermos-refractive noise remains a hurdle, requiring additional correction mechanisms, such as a blue-detuned auxiliary laser, albeit at the cost of increased complexity and power consumption.

Electro-optic comb generators offer agile mode spacing tuning and find applications in precision metrology and astronomical spectrograph calibration. Supercontinuum generation in photonic waveguides has overcome challenges associated with low pulse energies in certain OFC platforms, presenting a breakthrough in achieving pulse energies lower than 200 pJ. Recent progress in chip-based nonlinear photonics has enabled the development of compact, portable, and fully integrated comb devices, holding great potential for diverse applications. OFC devices with wide bandwidths are particularly valuable for applications like spectroscopy and time and frequency metrology, especially when employing self-referencing via  $f-2f$  interferometry. Supercontinuum Generation (SCG) in optical waveguides and Kerr-comb Generation (KCG) in micro-resonators are prominent methods for achieving broad spectral bandwidths [8, 238–244]. Supercontinuum Generation exploits nonlinear effects in a waveguide to generate a broad comb-like spectrum with evenly spaced frequency components [244–246].

On the other hand, KCG utilizes the Kerr effect, induced by changes in a material's refractive index with light intensity, to create equidistant frequency components across a broad spectrum using micro-resonators. The Kerr nonlinearity within a high-quality (high-Q) micro-resonator can lead to the formation of soliton pulses, resulting in a comb of equidistant spectral lines. Kippenberg et al. [247] report the first observation of Kerr nonlinearity-induced optical parametric oscillation in a microcavity, using geometrical control of toroid microcavities. This work holds significant implications for the potential realization of Kerr-based optical frequency comb (OFC) generation on a chip. Integrated photonics Kerr combs with octave-spanning Optical Frequency Combs (OFCs) have been demonstrated, enabling essential self-reference at  $f-2f$  [239, 248–250]. Savchenkov et al. [251] demonstrated low-

threshold optical parametric oscillations in a high-Q fluorite whispering gallery mode resonator, stemming from resonantly enhanced four-wave mixing attributed to Kerr nonlinearity [245]. They present the optical parametric oscillations in a high-Q  $CaF_2$  crystalline resonator, demonstrating the efficient generation of narrow-band optical sidebands for an all-optical frequency reference. Kerr combs in micro-resonators have been achieved using various materials, including silica ( $SiO_2$ ) [238, 247, 252–254], silicon nitride (SiN) [226, 255–258], Si [238, 259], aluminum nitride (AlN) [238, 260], and aluminum-gallium arsenide (AlGaAs) [238, 261].

Integrated photonic on-chip frequency combs have attracted interest in building sensing systems for various applications, detecting various gases, environmental monitoring, and medical diagnostics. In recent years, advancements in on-chip gas sensors utilizing continuous lasers have been shown [141, 148, 262, 263]. However, the simultaneous detection of multiple gases remains a challenge. Addressing this, Gangyun Guan et al. [262] have designed an integrated photonic multicomponent gas sensor using a microcavity Kerr frequency comb, enabling multiplexed gas sensing for water vapor ( $H_2O$ ), ammonia ( $NH_3$ ), acetylene ( $C_2H_2$ ), and carbon dioxide ( $CO_2$ ) within the 1-2  $\mu m$  range. The sensor features a symmetric double-ring microcavity with a feedback structure for Dispersive Kerr Soliton generation and a long sensing waveguide to achieve adequate absorption in the NIR wavelengths (see Fig. 13(a-b)). Their study marked the inception of an integrated Kerr frequency comb for on-chip gas sensing, showcasing remarkable stability and sensing performance evaluations with the promise of ppmv level sensitivity.

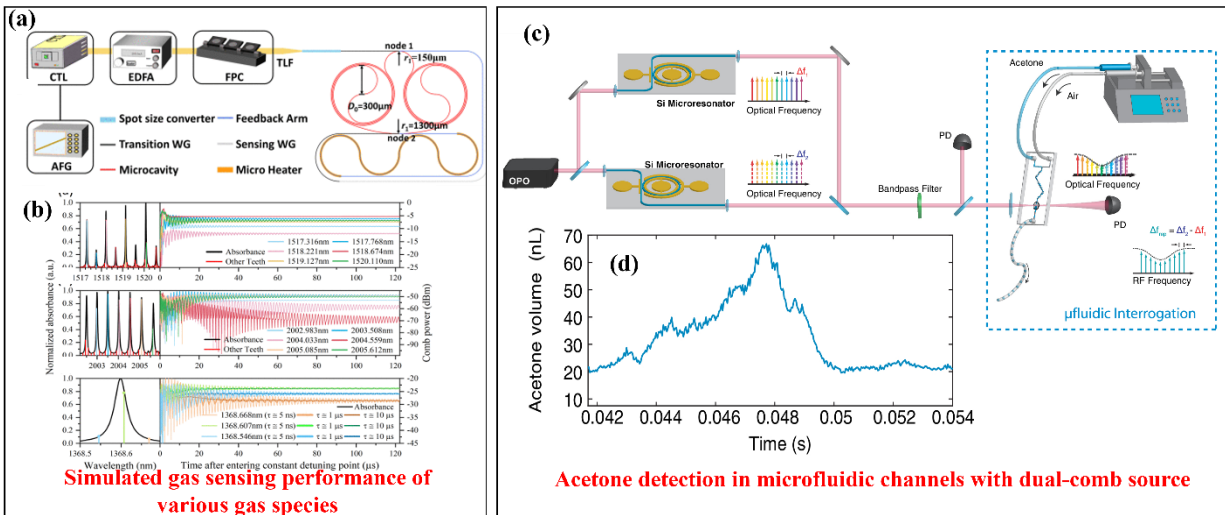


Figure 13 (a) Schematic of on-chip multi-gas sensor using dissipative Kerr soliton combs. (b) Analysis of power and thermal stability of optical frequency comb teeth. Absorption spectra of gases and power fluctuations. (c) Experimental setup: Continuous-wave OPO splits to pump silicon micro-resonators for mid-IR frequency combs generation. Outputs are combined, filtered, and split into reference and sample arms. Acetone droplets are introduced via a microfluidic chip. (d) Calculated acetone volume detected over time with 40  $\mu s$  temporal resolution. [264]

Mengjie Yu et al. [264] presented micro-resonator-based soliton combs utilizing a microfluidic chip-based dual-comb spectroscopy (DCS) method (Fig. 13 (c-d)) for real-time probing of linear absorption in liquid acetone within the mid-infrared range (2900 nm to 2990 nm). Notably, the experiment achieves a high spectral acquisition rate of 25 kHz, providing insights into acetone droplet dynamics, and showing compact time-resolved spectroscopy systems applicable in various sensing and imaging domains such as chemistry, biology, and industry. Heterogeneous integration of  $Si_3N_4$ -based micro-resonators and III-V semiconductor lasers promise cost-effective mass production of frequency comb chips. Progress in self-

injection locking and nonlinear effects drives optical frequency combs from laboratories toward market applications. Integrating key components holds potential for super-miniaturized, fully on-chip direct frequency comb sensing spectral chips, facilitating the practical use of optical frequency combs in various applications.

Table 4 offers a concise overview of the capabilities and performance metrics of on-chip spectroscopic methods. It facilitates comparing and understanding their potential applications across various domains, from environmental monitoring to biomedical diagnostics.

Table 4: State-of-art derived from diverse on-chip spectroscopy techniques.

Spectroscopy type	Wavelength(s)	Sensitivity	LOD/resolution	Analyte detected/targeted
DAS	6.19 $\mu\text{m}$	0.075-92 mg/ml		BSA [149]
DAS	3.291 4.319 and 7.625 $\mu\text{m}$		5.9 ppm	$\text{CH}_4$ and $\text{CO}_2$ [265]
DAS	3.3 and 3.6 $\mu\text{m}$			Hexane and ethanol vapor [147]
TDLAS	2.566 $\mu\text{m}$	7 ppm		$\text{C}_2\text{H}_2$ [141]
FTS	3.7-4.05 $\mu\text{m}$		3 nm (resolution limit)	$\text{N}_2\text{O}$ spectrum reconstruction [160]
DCS	2.6 to 4.1 $\mu\text{m}$		4.2 $\text{cm}^{-1}$ (resolution)	Acetone (liquid phase) [266]
WMS	3.291 $\mu\text{m}$	348 ppm		Methane [267]

## 5 Enhancing On-Chip Biosensor Performance with Artificial Intelligence/Machine Learning Algorithms

Artificial intelligence (AI) and machine learning (ML) play a crucial role in enhancing the functionality and performance of on-chip biosensors. These technologies enable the efficient analysis of complex biological data generated by biosensors, aiding in the rapid and accurate detection of biomolecules. AI algorithms can recognize patterns, identify trends, and make predictions based on sensor data, leading to improved sensitivity and specificity in identifying new biomarkers and detecting known biological targets. ML models can adapt and optimize sensor parameters, enhancing overall system efficiency. Moreover, AI facilitates real-time monitoring, interpretation of dynamic biological responses, and the development of intelligent, autonomous biosensing systems. Integrating AI and ML with on-chip biosensors is promising for advancing diagnostic capabilities and personalized healthcare applications.

In this section, we provide a concise explanation of various AI/ML types. Our primary goal is to enhance the efficiency of on-chip biosensors by integrating AI/ML, aiming to precisely articulate the conclusions derived from it and comprehend potential patterns. Commonly used AI/ML approaches include supervised learning, unsupervised learning, and reinforcement learning. Supervised learning, which involves training a model on labeled datasets, is well-suited for applications where historical data with clear outcomes are available, such as in the quantitative analysis of biomolecules [268, 269]. Unsupervised learning, on the other hand, is beneficial for clustering and pattern recognition tasks, making it suitable for identifying unknown patterns or anomalies in biosensor data [270]. However, one drawback of unsupervised learning models lies in their 'black box' nature, where the specific features the model focuses on remain unknown. This becomes particularly significant in clinical settings, where identifying these features could offer opportunities for biomarker discovery and diagnostic applications. However, it is essential to invest effort in comprehending the inner workings of the model to ensure scientific validation before considering its clinical utility. Reinforcement learning, known for decision-making in dynamic environments, can be applied in biosensor applications requiring adaptive responses to changing conditions [271]. The choice of the most appropriate AI/ML approach depends on the specific

requirements and characteristics of the on-chip biosensor application. Criteria for selection include the availability of labeled data, the complexity of the analysis, and the desired level of interpretability. Steps to adopt different types of AI/ML involve defining the problem, collecting and preprocessing data, selecting a suitable algorithm, training the model, and evaluating its performance. Continuous refinement and adaptation of the chosen AI/ML technique are essential to ensure optimal results in the dynamic context of on-chip biosensors.

When evaluating different types of AI/ML techniques for on-chip biosensor applications, the selection criteria are contingent upon various factors. These include the nature of the data, where the data type plays a crucial role. Image and complex graphical data might necessitate convolutional neural networks (CNNs) [272–274]. For instance, a one-dimensional CNN is applied to recognize absorption spectra in mixtures featuring 64 predefined mixing ratios. The classification accuracy attains 98.88%, particularly in the analysis of aqueous mixtures within the mid-infrared (MIR) using the Si-metamaterial waveguide sensing platform [275]. Alternatively, random forest [276] and XGBoost [277] are widely utilized models for effectively handling tabular data. Recently, Robison et al. developed a 13-plex immunoassay panel to assess cytokine release from peripheral blood mononuclear cells stimulated with Mycobacterium tuberculosis-relevant antigens. This study encompasses 65 subjects with diverse TB exposure risks and utilized Random Forest feature selection to identify cytokine biomarkers [278] detected using silicon photonic micro-ring sensor arrays.

Additionally, the size of the dataset is pivotal, as deep learning models often require large datasets for training, whereas simpler models may only suffice with smaller datasets [279]. Feature selection is another critical consideration, involving the identification of pertinent variables for model training. Furthermore, the pre-processing steps, such as data cleaning, denoising, and transformation, must align with the specific characteristics of the data. Common preprocessing techniques include derivatives, denoising, Fourier transform, among others. System-specific preprocessing methods encompass data compression, baseline drift elimination, normalization, transformations, and similar techniques. The adoption of preprocessing methods profoundly influences the overall performance of ML models. In the context of Raman spectroscopy, each spectrum necessitates Savitsky-Golay smoothing, background subtraction, and normalized min-max scaling [280]. This standardized preprocessing ensures the data is appropriately refined for optimal performance within ML models. Post-processing steps, applied after obtaining predictions, may be essential for refining or interpreting results.

Biosensors often generate time-dependent data, such as continuous monitoring of physiological parameters, dynamic responses to stimuli, or sequential molecular interactions. The architecture of the chosen model is paramount, with considerations like recurrent neural networks (RNNs) for such sequential data. Zhang et al. used RNNs for quantifying microRNA with theory-guided supervision to improve classification metrics by 13.8%, achieving 98.5% accuracy in (let-7a) concentrations on cantilever biosensors, reducing false results [281].

Support Vector Machines (SVM) are widely used in biosensor applications, particularly for classification tasks, due to their effectiveness in handling high-dimensional data and binary classification problems. Rong et al. employ multilayer perceptron (MLP) and SVM to process signals from a COVID-19 optical-based detector on top of the nanoporous silicon material-based biosensor. The study demonstrated qualitatively detecting SARS-CoV-2 with concentrations as low as 1 TCID<sub>50</sub>/mL. By analyzing data distribution patterns using T-distributed stochastic neighbor embedding (t-SNE) [282].

An Artificial Neural Network (ANN) is a computational model designed based on the structure and operation of the human brain. It comprises interconnected nodes arranged in layers—input, hidden, and output. The connections between nodes possess weights that are tuned during training, allowing the network to acquire knowledge and perform predictions or classifications. ANNs possess the capability to grasp intricate patterns and associations in data, proving effective for tasks like classification, regression, and pattern recognition. They demonstrate proficiency in managing non-linear relationships and adjusting to varied and high-dimensional datasets. Utilizing ANNs, Hamed et al. reported a nanophotonic biosensor to accurately predict electrical signal outputs, demonstrating superior performance ( $MSE \approx 2.9 \times 10^{-8}$ ) compared to finite-difference time-domain (FDTD) methods. The ANN model, with inputs

including biosample refractive index, central wavelength, and FWHM, enables efficient pre-optimization for sensitivity and responsivity, revealing optimal conditions for a 735 nm central wavelength and 70 nm FWHM light source [283].

It is worth noticing that most neural networks are electronic-based because traditional implementations leverage digital electronic components, providing fast and efficient computation. Electronic circuits are well-suited for representing and manipulating the interconnected nodes and computations inherent in neural network architectures. Nevertheless, electric neural networks often consume substantial power and exhibit restricted parallelism in processing information, resulting in potential bottlenecks.

Diverging from conventional electronic-based neural networks, optical neural networks (ONNs) represent a state-of-the-art advancement exploiting light for intricate computations [284, 285], inspired by the intricate connections in our brain. Leveraging the inherent parallelism and swift nature of light, ONNs aim to accelerate AI and machine learning tasks. These networks ingeniously leverage light's distinctive characteristics, including interference, diffraction, and polarization, for collective calculations, thereby markedly enhancing processing speed and capacity [286]. However, several unresolved issues need addressing before fully harnessing the potential of optical neural networks (ONNs). For instance, although matrix multiplication is accomplished optically in ONNs, the subsequent application of activation functions still relies on electrical processes, limiting the overall speed advantages of ONNs. Another challenge is the absence of a fully optical feedback loop in ONNs, hindering the operation of models such as recurrent neural networks that require recurrent connections for sequential data processing. These challenges underscore the need for further advancements to fully exploit the capabilities of optical neural networks.

In the area of bio-sensing, ONNs emerge as a game-changing technology poised to reshape the narrative of biological molecule detection, analysis, and interpretation [287–289]. Fusing ONNs with bio-sensing platforms ushers in a myriad of advantages. Primarily, ONNs wield heightened sensitivity and pinpoint accuracy, empowering the detection of laser modulation frequency or analyte concentrations concealed within intricate biological samples. This precision proves pivotal for early ailment identification, personalized healthcare, and ecological monitoring. Moreover, ONNs' parallel processing prowess fast-tracks data scrutiny, leading to real-time monitoring and swift decision-making—particularly pivotal in scenarios like point-of-care testing, where prompt outcomes are instrumental for timely intervention.

## **6 Conclusion**

In a harmonious convergence of scientific ingenuity and technological prowess, the field of on-chip sensing has witnessed a profound transformation, propelled by advancements in optical micro-ring resonators, photonic crystal waveguides, and integrated photonics. These miniature marvels, exploiting the intricate interplay between light and matter, herald a new era of sensing capabilities across a myriad of domains. Through meticulous expertise and theoretical insight, researchers have unlocked and are continuously exploring the latent potential of these platforms, unveiling unprecedented sensitivity and selectivity in discerning molecular intricacies. This convergence of cutting-edge science and visionary engineering foreshadows a paradigm shift in our quest for understanding and stewardship of the world around us. With unwavering dedication and collaborative endeavor, the journey towards realizing the full potential of on-chip optical sensing unfolds, illuminating a future where the boundless possibilities of light illuminate our path forward. Furthermore, the evolution of on-chip spectroscopic sensing, encompassing absorption-based spectroscopy, Fourier Transform Spectrometers, and Wavelength Modulation Spectroscopy, marks a pivotal advancement with transformative potential across diverse applications. Leveraging photonic devices, these techniques offer compact and portable solutions for environmental monitoring, biomedical diagnostics, and beyond. While challenges persist in enhancing interaction length and environmental robustness, recent developments underscore the promise of on-chip spectroscopic sensing in revolutionizing scientific exploration and technological innovation. Simultaneously, the integration of AI/ML algorithms with on-chip biosensors represents a significant leap forward, enabling enhanced sensitivity, specificity, and real-time monitoring capabilities. Through tailored AI/ML approaches, biosensors can efficiently analyze complex biological data, leading to rapid

biomolecule detection and biomarker identification. The emergence of Optical Neural Networks further accelerates biosensing tasks, promising heightened accuracy and real-time monitoring for personalized healthcare, disease detection, and environmental monitoring.

**Authors' Contributions:** Sourabh Jain and May Hlaing contributed equally to this work.

**Funding:** The authors acknowledge support from NASA and DOE under contract numbers NASA-80NSSC22PB125, DE-SC0023917 and DE-SC0024015.

## References:

- [1] N. M. Jokerst, L. Luan, S. Palit, M. Royal, S. Dhar, M. Brooke, and T. Tyler II, "Progress in chip-scale photonic sensing," *IEEE transactions on biomedical circuits and systems*, vol. 3, no. 4, pp. 202–211, 2009.
- [2] E. Pelucchi, G. Fagas, I. Aharonovich, D. Englund, E. Figueroa, Q. Gong, H. Hannes, J. Liu, C.-Y. Lu, N. Matsuda, et al., "The potential and global outlook of integrated photonics for quantum technologies," *Nature Reviews Physics*, vol. 4, no. 3, pp. 194–208, 2022.
- [3] B. Jalali and S. Fathpour, "Silicon photonics," *Journal of lightwave technology*, vol. 24, no. 12, pp. 4600–4615, 2006.
- [4] A. Katiyi and A. Karabchevsky, "Figure of merit of all-dielectric waveguide structures for absorption overtone spectroscopy," *Journal of Lightwave Technology*, vol. 35, no. 14, pp. 2902–2908, 2017. [5] "<https://scholar.google.com/>."
- [6] I. F. Akyildiz, J. M. Jornet, and C. Han, "Terahertz band: Next frontier for wireless communications," *Physical communication*, vol. 12, pp. 16–32, 2014.
- [7] J. Xie, W. Ye, L. Zhou, X. Guo, X. Zang, L. Chen, and Y. Zhu, "A review on terahertz technologies accelerated by silicon photonics," *Nanomaterials*, vol. 11, no. 7, p. 1646, 2021.
- [8] X. Guo, X. Ji, B. Yao, T. Tan, A. Chu, O. Westreich, A. Dutt, C. Wong, and Y. Su, "Ultra-wideband integrated photonic devices on silicon platform: from visible to mid-ir," *Nanophotonics*, vol. 12, no. 2, pp. 167–196, 2023.
- [9] S. Arafin and L. A. Coldren, "Advanced in photonic integrated circuits for communication and sensing," *IEEE Journal of Selected Topics in Quantum Electronics*, vol. 24, no. 1, pp. 1–12, 2017.
- [10] R. Soref, "Mid-infrared photonics in silicon and germanium," *Nature photonics*, vol. 4, no. 8, pp. 495–497, 2010.
- [11] K. Ikeda, R. E. Saperstein, N. Alic, and Y. Fainman, "Thermal and kerr nonlinear properties of plasma-deposited silicon nitride/silicon dioxide waveguides," *Optics express*, vol. 16, no. 17, pp. 12987–12994, 2008.
- [12] L. Carroll, J.-S. Lee, C. Scarcella, K. Gradkowski, M. Duperron, H. Lu, Y. Zhao, C. Eason, P. Morrissey, M. Rensing, et al., "Photonic packaging: transforming silicon photonic integrated circuits into photonic devices," *Applied Sciences*, vol. 6, no. 12, p. 426, 2016.
- [13] P. Kaur, A. Boes, G. Ren, T. G. Nguyen, G. Roelkens, and A. Mitchell, "Hybrid and heterogeneous photonic integration," *APL Photonics*, vol. 6, no. 6, 2021.
- [14] J. Justice, C. Bower, M. Meitl, M. B. Mooney, M. A. Gubbins, and B. Corbett, "Wafer-scale integration of group iii–v lasers on silicon using transfer printing of epitaxial layers," *Nature Photonics*, vol. 6, no. 9, pp. 610–614, 2012.
- [15] H. Park, C. Zhang, M. A. Tran, and T. Komljenovic, "Heterogeneous silicon nitride photonics: erratum," *Optica*, vol. 7, no. 5, pp. 425–425, 2020.
- [16] S. Chakravarty, J. Midkiff, K. Yoo, C.-J. Chung, A. Rostamian, and R. T. Chen, "Compact integrated photonic components for  $\lambda = 3\text{--}15$  micron," in *Integrated Optics: Devices, Materials, and Technologies XXIII*, vol. 10921, p. 109210D, International Society for Optics and Photonics, 2019.
- [17] K. Ahmed, F. Ahmed, S. Roy, B. K. Paul, M. N. Aktar, D. Vigneswaran, and M. S. Islam, "Refractive index-based blood components sensing in terahertz spectrum," *IEEE Sensors Journal*, vol. 19, no. 9, pp. 3368–3375, 2019.

- [18] M. Danaie and B. Kiani, "Design of a label-free photonic crystal refractive index sensor for biomedical applications," *Photonics and nanostructures-fundamentals and applications*, vol. 31, pp. 89–98, 2018.
- [19] N. Kazanskiy, S. Khonina, and M. Butt, "Plasmonic sensors based on metal-insulator-metal waveguides for refractive index sensing applications: A brief review," *Physica E: Low-dimensional systems and nanostructures*, vol. 117, p. 113798, 2020.
- [20] C. Han, M. Jin, Y. Tao, B. Shen, and X. Wang, "Recent progress in silicon-based slow-light electro-optic modulators," *Micromachines*, vol. 13, no. 3, p. 400, 2022.
- [21] M. C. Estevez, M. Alvarez, and L. M. Lechuga, "Integrated optical devices for lab-on-a-chip biosensing applications," *Laser & Photonics Reviews*, vol. 6, no. 4, pp. 463–487, 2012.
- [22] M. C. Cardenosa-Rubio, H. M. Robison, and R. C. Bailey, "Recent advances in environmental and clinical analysis using microring resonator-based sensors," *Current opinion in environmental science & health*, vol. 10, pp. 38–46, 2019.
- [23] F. Vogelbacher, T. Kothe, P. Muellner, E. Melnik, M. Sagmeister, J. Kraft, and R. Hainberger, "Waveguide machzehnder biosensor with laser diode pumped integrated single-mode silicon nitride organic hybrid solid-state laser," *Biosensors and Bioelectronics*, vol. 197, p. 113816, 2022.
- [24] V. Vashistha, M. Krawczyk, A. E. Serebryannikov, and G. A. Vandenbosch, "Light guiding, bending, and splitting via local modification of interfaces of a photonic waveguide," *Optics Letters*, vol. 44, no. 19, pp. 4725–4728, 2019.
- [25] W. Bogaerts, P. De Heyn, T. Van Vaerenbergh, K. De Vos, S. Kumar Selvaraja, T. Claes, P. Dumon, P. Bienstman, D. Van Thourhout, and R. Baets, "Silicon microring resonators," *Laser & Photonics Reviews*, vol. 6, no. 1, pp. 47–73, 2012.
- [26] M. W. Puckett, K. Liu, N. Chauhan, Q. Zhao, N. Jin, H. Cheng, J. Wu, R. O. Behunin, P. T. Rakich, K. D. Nelson, et al., "422 million intrinsic quality factor planar integrated all-waveguide resonator with sub-mhz linewidth," *Nature communications*, vol. 12, no. 1, p. 934, 2021.
- [27] G. H. Ahn, K. Y. Yang, R. Trivedi, A. D. White, L. Su, J. Skarda, and J. Vučković, "Photonic inverse design of on-chip microresonators," *ACS Photonics*, vol. 9, no. 6, pp. 1875–1881, 2022.
- [28] B. E. Little, S. T. Chu, H. A. Haus, J. Foresi, and J.-P. Laine, "Microring resonator channel dropping filters," *Journal of lightwave technology*, vol. 15, no. 6, pp. 998–1005, 1997.
- [29] R. Schilling, C. Xiong, S. Kamapurkar, A. Falk, N. Marchack, S. Bedell, R. Haight, C. Scerbo, H. Paik, and J. S. Orcutt, "Ultrahigh-q on-chip silicon-germanium microresonators," *Optica*, vol. 9, no. 3, pp. 284–287, 2022.
- [30] K. Liu, N. Jin, H. Cheng, N. Chauhan, M. W. Puckett, K. D. Nelson, R. O. Behunin, P. T. Rakich, and D. J. Blumenthal, "Ultralow 0.034 db/m loss wafer-scale integrated photonics realizing 720 million q and 380  $\mu$ w threshold brillouin lasing," *Optics letters*, vol. 47, no. 7, pp. 1855–1858, 2022.
- [31] K. Padmaraju, J. Chan, L. Chen, M. Lipson, and K. Bergman, "Thermal stabilization of a microring modulator using feedback control," *Optics express*, vol. 20, no. 27, pp. 27999–28008, 2012.
- [32] L. Zhou, X. Sun, X. Li, and J. Chen, "Miniature microring resonator sensor based on a hybrid plasmonic waveguide," *Sensors*, vol. 11, no. 7, pp. 6856–6867, 2011.
- [33] S. Ning, H.-C. Chang, K.-C. Fan, M. H. Hlaing, S. Jain, J. Carmichael, L. Head, D. Goswami, S. Sriwattana, H. Pietsch, et al., "Silicon photonic chip-based biosensor for covid-19 and flu detection with high sensitivity and specificity," in *Ultra-High-Definition Imaging Systems VI*, vol. 12444, pp. 26–28, SPIE, 2023.
- [34] X. Xu, Z. Pan, C.-J. Chung, C.-W. Chang, H. Yan, and R. T. Chen, "Subwavelength grating metamaterial racetrack resonator for sensing and modulation," *IEEE Journal of Selected Topics in Quantum Electronics*, vol. 25, no. 3, pp. 1–8, 2019.
- [35] S. M. Lo, S. Hu, G. Gaur, Y. Kostoulas, S. M. Weiss, and P. M. Fauchet, "Photonic crystal microring resonator for label-free biosensing," *Optics express*, vol. 25, no. 6, pp. 7046–7054, 2017.
- [36] S. Ning, H.-C. Chang, K.-C. Fan, P.-y. Hsiao, C. Feng, D. Shoemaker, and R. T. Chen, "A point-of-care biosensor for rapid detection and differentiation of covid-19 virus (sars-cov-2) and influenza virus using subwavelength grating micro-ring resonator," *Applied Physics Reviews*, vol. 10, no. 2, 2023.

- [37] H. Yan, L. Huang, X. Xu, S. Chakravarty, N. Tang, H. Tian, and R. T. Chen, "Unique surface sensing property and enhanced sensitivity in microring resonator biosensors based on subwavelength grating waveguides," *Optics express*, vol. 24, no. 26, pp. 29724–29733, 2016.
- [38] Z. Wang, X. Xu, D. Fan, Y. Wang, H. Subbaraman, and R. T. Chen, "Geometrical tuning art for entirely subwavelength grating waveguide based integrated photonics circuits," *Scientific reports*, vol. 6, no. 1, p. 24106, 2016.
- [39] Z. Wang, X. Xu, D. Fan, Y. Wang, and R. T. Chen, "High quality factor subwavelength grating waveguide microring resonator based on trapezoidal silicon pillars," *Optics letters*, vol. 41, no. 14, pp. 3375–3378, 2016.
- [40] F. Sun, B. Dong, J. Wei, Y. Ma, H. Tian, and C. Lee, "Demonstration of mid-infrared slow light one-dimensional photonic crystal ring resonator with high-order photonic bandgap," *Optics Express*, vol. 28, no. 21, pp. 30736–30747, 2020.
- [41] J. Wang, S. X. Chew, S. Song, L. Li, L. Nguyen, and X. Yi, "On-chip simultaneous measurement of humidity and temperature using cascaded photonic crystal microring resonators with error correction," *Optics Express*, vol. 30, no. 20, pp. 35608–35623, 2022.
- [42] J.-H. Kim, S. Aghaeimeibodi, J. Carolan, D. Englund, and E. Waks, "Hybrid integration methods for on-chip quantum photonics," *Optica*, vol. 7, no. 4, pp. 291–308, 2020.
- [43] A. W. Elshaari, W. Pernice, K. Srinivasan, O. Benson, and V. Zwiller, "Hybrid integrated quantum photonic circuits," *Nature Photonics*, vol. 14, no. 5, pp. 285–298, 2020.
- [44] G. Moody, V. J. Sorger, D. J. Blumenthal, P. W. Juodawlkis, W. Loh, C. Sorace-Agaskar, A. E. Jones, K. C. Balram, J. C. Matthews, A. Laing, et al., "2022 roadmap on integrated quantum photonics," *Journal of Physics: Photonics*, vol. 4, no. 1, p. 012501, 2022.
- [45] C.-B. Yu, Y. Wu, X.-L. Liu, B.-C. Yao, F. Fu, Y. Gong, Y.-J. Rao, and Y.-F. Chen, "Graphene oxide deposited microfiber knot resonator for gas sensing," *Optical Materials Express*, vol. 6, no. 3, pp. 727–733, 2016.
- [46] G. Ren, B. Y. Zhang, Q. Yao, A. Zavabeti, C. S. Huertas, R. Brkljača, M. W. Khan, H. Nili, R. S. Datta, H. Khan, et al., "An ultrasensitive silicon photonic ion sensor enabled by 2d plasmonic molybdenum oxide," *Small*, vol. 15, no. 9, p. 1805251, 2019.
- [47] Z. Cheng, R. Cao, K. Wei, Y. Yao, X. Liu, J. Kang, J. Dong, Z. Shi, H. Zhang, and X. Zhang, "2d materials enabled next-generation integrated optoelectronics: from fabrication to applications," *Advanced Science*, vol. 8, no. 11, p. 2003834, 2021.
- [48] R. Kou, Y. Kobayashi, S. Inoue, T. Tsuchizawa, Y. Ueno, S. Suzuki, H. Hibino, T. Yamamoto, H. Nakajima, and K. Yamada, "Dopamine detection on activated reaction field consisting of graphene-integrated silicon photonic cavity," *Optics Express*, vol. 27, no. 22, pp. 32058–32068, 2019.
- [49] X. Wu, J. Wang, J. Han, Y. Xie, X. Ge, J. Liao, and Y. Yi, "Design of suspended slot racetrack microring refractive index sensor based on polymer nanocomposite," *Polymers*, vol. 15, no. 9, p. 2113, 2023.
- [50] Z. Cheng and K. Goda, "Design of waveguide-integrated graphene devices for photonic gas sensing," *Nanotechnology*, vol. 27, no. 50, p. 505206, 2016.
- [51] J. Wang, Y. Chen, Y. Geng, X. Hong, and X. Li, "Theoretical design of mid-infrared graphene optical gas sensor based on slot si core fiber," *IEEE Photonics Technology Letters*, vol. 31, no. 13, pp. 1096–1099, 2019.
- [52] K. De Vos, I. Bartolozzi, E. Schacht, P. Bienstman, and R. Baets, "Silicon-on-insulator microring resonator for sensitive and label-free biosensing," *Optics express*, vol. 15, no. 12, pp. 7610–7615, 2007.
- [53] S. T. Fard, V. Donzella, S. A. Schmidt, J. Flueckiger, S. M. Grist, P. T. Fard, Y. Wu, R. J. Bojko, E. Kwok, N. A. Jaeger, et al., "Performance of ultra-thin soi-based resonators for sensing applications," *Optics express*, vol. 22, no. 12, pp. 14166–14179, 2014.
- [54] V. Soni, C.-W. Chang, X. Xu, C. Wang, H. Yan, M. D'Agati, L.-W. Tu, Q. Y. Chen, H. Tian, and R. T. Chen, "Portable automatic microring resonator system using a subwavelength grating metamaterial waveguide for high sensitivity real-time optical-biosensing applications," *IEEE Transactions on Biomedical Engineering*, vol. 68, no. 6, pp. 1894–1902, 2020.



- [55] J. D. Joannopoulos, P. R. Villeneuve, and S. Fan, "Photonic crystals," *Solid State Communications*, vol. 102, no. 2-3, pp. 165–173, 1997.
- [56] K. Busch, S. Lölkes, R. B. Wehrspohn, and H. Föll, *Photonic crystals: advances in design, fabrication, and characterization*. John Wiley & Sons, 2006.
- [57] M. Soljačić and J. D. Joannopoulos, "Enhancement of nonlinear effects using photonic crystals," *Nature materials*, vol. 3, no. 4, pp. 211–219, 2004.
- [58] A. Rostamian, E. Madadi-Kandjani, H. Dalir, V. J. Sorger, and R. T. Chen, "Towards lab-on-chip ultrasensitive ethanol detection using photonic crystal waveguide operating in the mid-infrared," *Nanophotonics*, vol. 10, no. 6, pp. 1675–1682, 2021.
- [59] D. Dorfner, T. Zabel, T. Hürlimann, N. Hauke, L. Frandsen, U. Rant, G. Abstreiter, and J. Finley, "Photonic crystal nanostructures for optical biosensing applications," *Biosensors and Bioelectronics*, vol. 24, no. 12, pp. 3688–3692, 2009.
- [60] C.-J. Yang, H. Yan, N. Tang, Y. Zou, Y. Al-Hadeethi, X. Xu, H. Dalir, and R. T. Chen, "Ultra sensitivity silicon-based photonic crystal microcavity biosensors for plasma protein detection in patients with pancreatic cancer," *Micromachines*, vol. 11, no. 3, p. 282, 2020.
- [61] L. Torrijos-Morán, A. Griol, and J. García-Rupérez, "Slow light bimodal interferometry in one-dimensional photonic crystal waveguides," *Light: Science & Applications*, vol. 10, no. 1, p. 16, 2021.
- [62] S. Jain, S. Srivastava, S. Rajput, L. Singh, P. Tiwari, A. K. Srivastava, and M. Kumar, "Thermally stable optical filtering using silicon-based comb-like asymmetric grating for sensing applications," *IEEE Sensors Journal*, vol. 20, no. 7, pp. 3529–3535, 2019.
- [63] F. Wu, T. Liu, M. Chen, and S. Xiao, "Photonic bandgap engineering in hybrid one-dimensional photonic crystals containing all-dielectric elliptical metamaterials," *Optics Express*, vol. 30, no. 19, pp. 33911–33925, 2022.
- [64] S. Jain, M. H. Hlaing, J. D. Shin, J. Midkiff, K. M. Yoo, A. Rostamian, and R. T. Chen, "Slow-light assisted and wavelength tunable tm waveguide on qcl/qcd compatible platform for mid-infrared lab-on-chip absorption spectroscopy," in *Optical Interconnects XXII*, vol. 12007, pp. 43–48, SPIE, 2022.
- [65] M. Scullion, A. Di Falco, and T. Krauss, "Slotted photonic crystal cavities with integrated microfluidics for biosensing applications," *Biosensors and Bioelectronics*, vol. 27, no. 1, pp. 101–105, 2011.
- [66] A. Bertoncini and C. Liberale, "3d printed waveguides based on photonic crystal fiber designs for complex fiber-end photonic devices," *Optica*, vol. 7, no. 11, pp. 1487–1494, 2020.
- [67] M. Notomi, "Manipulating light with strongly modulated photonic crystals," *Reports on Progress in Physics*, vol. 73, no. 9, p. 096501, 2010.
- [68] W.-C. Lai, S. Chakravarty, Y. Zou, and R. T. Chen, "Silicon nano-membrane based photonic crystal microcavities for high sensitivity bio-sensing," *Optics letters*, vol. 37, no. 7, pp. 1208–1210, 2012.
- [69] V. Toccafondo, J. García-Rupérez, M. Bañuls, A. Griol, J. Castelló, S. Peransi-Llopis, and A. Maquieira, "Singlestrand dna detection using a planar photonic-crystal-waveguide-based sensor," *Optics letters*, vol. 35, no. 21, pp. 3673–3675, 2010.
- [70] M. E. Stewart, C. R. Anderton, L. B. Thompson, J. Maria, S. K. Gray, J. A. Rogers, and R. G. Nuzzo, "Nanostructured plasmonic sensors," *Chemical reviews*, vol. 108, no. 2, pp. 494–521, 2008.
- [71] L. Singh, S. Jain, and M. Kumar, "Electrically writable silicon nanophotonic resistive memory with inherent stochasticity," *Optics letters*, vol. 44, no. 16, pp. 4020–4023, 2019.
- [72] C.-W. Cheng and S. Gwo, "Fundamentals of plasmonic materials," in *Plasmonic Materials and Metastructures*, pp. 3–33, Elsevier, 2024.
- [73] E. Kretschmann and H. Raether, "Radiative decay of non radiative surface plasmons excited by light," *Zeitschrift für Naturforschung A*, vol. 23, no. 12, pp. 2135–2136, 1968.
- [74] B. Liedberg, C. Nylander, and I. Lunström, "Surface plasmon resonance for gas detection and biosensing," *Sensors and actuators*, vol. 4, pp. 299–304, 1983.
- [75] J. Homola, S. S. Yee, and G. Gauglitz, "Surface plasmon resonance sensors," *Sensors and actuators B: Chemical*, vol. 54, no. 1-2, pp. 3–15, 1999.

- [76] J. Homola, "Surface plasmon resonance sensors for detection of chemical and biological species," *Chemical reviews*, vol. 108, no. 2, pp. 462–493, 2008.
- [77] J. Shang, G. Ye, K. Shi, Y. Wan, C. Luo, H. Aihara, Q. Geng, A. Auerbach, and F. Li, "Structural basis of receptor recognition by sars-cov-2," *Nature*, vol. 581, no. 7807, pp. 221–224, 2020.
- [78] I. Abdulhalim, M. Zourob, and A. Lakhtakia, "Surface plasmon resonance for biosensing: a mini-review," *Electromagnetics*, vol. 28, no. 3, pp. 214–242, 2008.
- [79] H. Zhang, Y. Chen, X. Feng, X. Xiong, S. Hu, Z. Jiang, J. Dong, W. Zhu, W. Qiu, H. Guan, et al., "Long-range surface plasmon resonance sensor based on side-polished fiber for biosensing applications," *IEEE Journal of Selected Topics in Quantum Electronics*, vol. 25, no. 2, pp. 1–9, 2018.
- [80] S. Rossi, E. Gazzola, P. Capaldo, G. Borile, and F. Romanato, "Grating-coupled surface plasmon resonance (gc-spr) optimization for phase-interrogation biosensing in a microfluidic chamber," *Sensors*, vol. 18, no. 5, p. 1621, 2018.
- [81] B. Douzi, "Protein–protein interactions: Surface plasmon resonance," *Bacterial Protein Secretion Systems: Methods and Protocols*, pp. 257–275, 2017.
- [82] O. Zagorodko, J. Spadavecchia, A. Y. Serrano, I. Larroulet, A. Pesquera, A. Zurutuza, R. Boukherroub, and S. Szunerits, "Highly sensitive detection of dna hybridization on commercialized graphene-coated surface plasmon resonance interfaces," *Analytical chemistry*, vol. 86, no. 22, pp. 11211–11216, 2014.
- [83] D. H. Siepe, L. T. Henneberg, S. C. Wilson, G. T. Hess, M. C. Bassik, K. Zinn, and K. C. Garcia, "Identification of orphan ligand-receptor relationships using a cell-based crispra enrichment screening platform," *Elife*, vol. 11, p. e81398, 2022.
- [84] L. He, Q. Pagneux, I. Larroulet, A. Y. Serrano, A. Pesquera, A. Zurutuza, D. Mandler, R. Boukherroub, and S. Szunerits, "Label-free femtomolar cancer biomarker detection in human serum using graphene-coated surface plasmon resonance chips," *Biosensors and Bioelectronics*, vol. 89, pp. 606–611, 2017.
- [85] H. Wang, X. Wang, J. Wang, W. Fu, and C. Yao, "A spr biosensor based on signal amplification using antibody-qd conjugates for quantitative determination of multiple tumor markers," *Scientific reports*, vol. 6, no. 1, p. 33140, 2016.
- [86] L. A. García-Hernández, E. Martínez-Martínez, D. Pazos-Solís, J. Aguado-Preciado, A. Dutt, A. U. Chávez-Ramírez, B. Korgel, A. Sharma, and G. Oza, "Optical detection of cancer cells using lab-on-a-chip," *Biosensors*, vol. 13, no. 4, p. 439, 2023.
- [87] A. M. Shrivastav, U. Cvelbar, and I. Abdulhalim, "A comprehensive review on plasmonic-based biosensors used in viral diagnostics," *Communications biology*, vol. 4, no. 1, p. 70, 2021.
- [88] T. Vairaperumal, C.-C. Huang, and P.-Y. Liu, "Optical nanobiosensor-based point-of-care testing for cardiovascular disease biomarkers," *ACS Applied Bio Materials*, 2023.
- [89] L. Huang, L. Ding, J. Zhou, S. Chen, F. Chen, C. Zhao, J. Xu, W. Hu, J. Ji, H. Xu, et al., "One-step rapid quantification of sars-cov-2 virus particles via low-cost nanoplasmonic sensors in generic microplate reader and point-of-care device," *Biosensors and Bioelectronics*, vol. 171, p. 112685, 2021.
- [90] H.-Y. Hsieh, R. Chang, Y.-Y. Huang, P.-H. Juan, H. Tahara, K.-Y. Lee, M.-H. Tsai, P.-K. Wei, H.-J. Sheen, Y.-J. Fan, et al., "Continuous polymerase chain reaction microfluidics integrated with a gold-capped nanoslit sensing chip for epstein-barr virus detection," *Biosensors and Bioelectronics*, vol. 195, p. 113672, 2022.
- [91] C. Zhang, Z. Liu, C. Cai, Z. Yang, and Z.-M. Qi, "Surface plasmon resonance gas sensor with a nanoporous gold film," *Optics Letters*, vol. 47, no. 16, pp. 4155–4158, 2022.
- [92] C. R. Basso, C. D. Malossi, A. Haisi, V. de Albuquerque Pedrosa, A. N. Barbosa, R. T. Grotto, and J. P. A. Junior, "Fast and reliable detection of sars-cov-2 antibodies based on surface plasmon resonance," *Analytical Methods*, vol. 13, no. 29, pp. 3297–3306, 2021.
- [93] K. Watanabe, K. Matsumoto, T. Ohgaki, I. Sakaguchi, N. Ohashi, S. Hishita, and H. Haneda, "Development of zno-based surface plasmon resonance gas sensor and analysis of uv irradiation effect on no<sub>2</sub> desorption from zno thin films," *Journal of the Ceramic Society of Japan*, vol. 118, no. 1375, pp. 193–196, 2010.

- [94] A. Srivastava and Y. Prajapati, "Performance analysis of silicon and blue phosphorene/mos 2 hetero-structure based spr sensor," *Photonic Sensors*, vol. 9, pp. 284–292, 2019.
- [95] S.-Y. Cho, Y. Lee, H.-J. Koh, H. Jung, J.-S. Kim, H.-W. Yoo, J. Kim, and H.-T. Jung, "Superior chemical sensing performance of black phosphorus: comparison with mos2 and graphene," *Advanced Materials*, vol. 28, no. 32, pp. 7020–7028, 2016.
- [96] K. M. Mayer and J. H. Hafner, "Localized surface plasmon resonance sensors," *Chemical reviews*, vol. 111, no. 6, pp. 3828–3857, 2011.
- [97] H. Yockell-Lelièvre, F. Lussier, and J.-F. Masson, "Influence of the particle shape and density of self-assembled gold nanoparticle sensors on lspr and sers," *The Journal of Physical Chemistry C*, vol. 119, no. 51, pp. 28577–28585, 2015.
- [98] M. Li, S. K. Cushing, and N. Wu, "Plasmon-enhanced optical sensors: a review," *Analyst*, vol. 140, no. 2, pp. 386–406, 2015.
- [99] S. Wu, Q.-j. Wang, X.-g. Yin, J.-q. Li, D. Zhu, S.-q. Liu, and Y.-y. Zhu, "Enhanced optical transmission: Role of the localized surface plasmon," *Applied Physics Letters*, vol. 93, no. 10, p. 101113, 2008.
- [100] E. Petryayeva and U. J. Krull, "Localized surface plasmon resonance: Nanostructures, bioassays and biosensing—a review," *Analytica chimica acta*, vol. 706, no. 1, pp. 8–24, 2011.
- [101] K. Takemura, "Surface plasmon resonance (spr)-and localized spr (lspr)-based virus sensing systems: Optical vibration of nano-and micro-metallic materials for the development of next-generation virus detection technology," *Biosensors*, vol. 11, no. 8, p. 250, 2021.
- [102] M. Sharifi, B. Khalilzadeh, F. Bayat, I. Isildak, and H. Tajalli, "Application of thermal annealing-assisted gold nanoparticles for ultrasensitive diagnosis of pancreatic cancer using localized surface plasmon resonance," *Microchemical Journal*, vol. 190, p. 108698, 2023.
- [103] G. Qiu, Z. Gai, Y. Tao, J. Schmitt, G. A. Kullak-Ublick, and J. Wang, "Dual-functional plasmonic photothermal biosensors for highly accurate severe acute respiratory syndrome coronavirus 2 detection," *ACS nano*, vol. 14, no. 5, pp. 5268–5277, 2020.
- [104] F. A. A. Nugroho, P. Bai, I. Darmadi, G. W. Castellanos, J. Fritzsche, C. Langhammer, J. Gómez Rivas, and A. Baldi, "Inverse designed plasmonic metasurface with parts per billion optical hydrogen detection," *Nature Communications*, vol. 13, no. 1, p. 5737, 2022.
- [105] X. Wang, Y. Li, H. Wang, Q. Fu, J. Peng, Y. Wang, J. Du, Y. Zhou, and L. Zhan, "Gold nanorod-based localized surface plasmon resonance biosensor for sensitive detection of hepatitis b virus in buffer, blood serum and plasma," *Biosensors and Bioelectronics*, vol. 26, no. 2, pp. 404–410, 2010.
- [106] A. M. Ghanim, A. Yossry, and M. A. Swillam, "Mid-infrared localized surface plasmon resonances in silicon-dioxide nanoantennas for ozone detection," in *Integrated Optics: Design, Devices, Systems and Applications VII*, vol. 12575, pp. 116–120, SPIE, 2023.
- [107] A. Philip and A. R. Kumar, "The performance enhancement of surface plasmon resonance optical sensors using nanomaterials: A review," *Coordination Chemistry Reviews*, vol. 458, p. 214424, 2022.
- [108] P. L. Stiles, J. A. Dieringer, N. C. Shah, and R. P. Van Duyne, "Surface-enhanced raman spectroscopy," *Annu. Rev. Anal. Chem.*, vol. 1, pp. 601–626, 2008.
- [109] X. X. Han, R. S. Rodriguez, C. L. Haynes, Y. Ozaki, and B. Zhao, "Surface-enhanced raman spectroscopy," *Nature Reviews Methods Primers*, vol. 1, no. 1, p. 87, 2021.
- [110] M. Fleischmann, P. J. Hendra, and A. J. McQuillan, "Raman spectra of pyridine adsorbed at a silver electrode," *Chemical physics letters*, vol. 26, no. 2, pp. 163–166, 1974.
- [111] M. G. Albrecht and J. A. Creighton, "Anomalously intense raman spectra of pyridine at a silver electrode," *Journal of the american chemical society*, vol. 99, no. 15, pp. 5215–5217, 1977.
- [112] H. Marks, M. Schechinger, J. Garza, A. Locke, and G. Coté, "Surface enhanced raman spectroscopy (sers) for in vitro diagnostic testing at the point of care," *Nanophotonics*, vol. 6, no. 4, pp. 681–701, 2017.
- [113] H. Xu, X.-H. Wang, M. P. Persson, H. Xu, M. Käll, and P. Johansson, "Unified treatment of fluorescence and raman scattering processes near metal surfaces," *Physical review letters*, vol. 93, no. 24, p. 243002, 2004.

- [114] H. Xu, J. Aizpurua, M. Käll, and P. Apell, “Electromagnetic contributions to single-molecule sensitivity in surface-enhanced raman scattering,” *Physical Review E*, vol. 62, no. 3, p. 4318, 2000.
- [115] E. Babich, A. Redkov, I. Reduto, and A. Lipovskii, “Self-assembled silver–gold nanoisland films on glass for sers applications,” *physica status solidi (RRL)–Rapid Research Letters*, vol. 12, no. 1, p. 1700226, 2018.
- [116] K. Yuan, Q. Mei, X. Guo, Y. Xu, D. Yang, B. J. Sánchez, B. Sheng, C. Liu, Z. Hu, G. Yu, et al., “Antimicrobial peptide based magnetic recognition elements and Au@ Ag-GO SERS tags with stable internal standards: a three in one biosensor for isolation, discrimination and killing of multiple bacteria in whole blood,” *Chemical Science*, vol. 9, no. 47, pp. 8781–8795, 2018.
- [117] M. A. Tahir, N. E. Dina, H. Cheng, V. K. Valev, and L. Zhang, “Surface-enhanced raman spectroscopy for bioanalysis and diagnosis,” *Nanoscale*, vol. 13, no. 27, pp. 11593–11634, 2021.
- [118] T.-Y. Liu, K.-T. Tsai, H.-H. Wang, Y. Chen, Y.-H. Chen, Y.-C. Chao, H.-H. Chang, C.-H. Lin, J.-K. Wang, and Y.-L. Wang, “Functionalized arrays of raman-enhancing nanoparticles for capture and culture-free analysis of bacteria in human blood,” *Nature communications*, vol. 2, no. 1, p. 538, 2011.
- [119] S. Bai, X. Ren, K. Obata, Y. Ito, and K. Sugioka, “Label-free trace detection of bio-molecules by liquid-interface assisted surface-enhanced raman scattering using a microfluidic chip,” *Opto-Electronic Advances*, vol. 5, no. 10, pp. 210121–1, 2022.
- [120] B. Hu, D.-W. Sun, H. Pu, and Z. Huang, “High-performance homogeneous carboxymethylcellulose-stabilized au@ ag nrs-cmc surface-enhanced raman scattering chip for thiram detection in fruits,” *Food Chemistry*, vol. 412, p. 135332, 2023.
- [121] U. Eleteigerra, J. Martinez-Perdiguero, R. Barderas, J. M. Pingarrón, S. Campuzano, and S. Merino, “Surface plasmon resonance immunosensor for erbb2 breast cancer biomarker determination in human serum and raw cancer cell lysates,” *Analytica Chimica Acta*, vol. 905, pp. 156–162, 2016.
- [122] J. Zhou, Y. Wang, Y. Qian, T. Zhang, L. Zheng, and L. Fu, “Quantification of shellfish major allergen tropomyosin by spr biosensor with gold patterned biochips,” *Food Control*, vol. 107, p. 106547, 2020.
- [123] H. Xiong, Z. Huang, Q. Lin, B. Yang, F. Yan, B. Liu, H. Chen, and J. Kong, “Surface plasmon coupling electrochemiluminescence immunosensor based on polymer dots and aunps for ultrasensitive detection of pancreatic cancer exosomes,” *Analytical Chemistry*, vol. 94, no. 2, pp. 837–846, 2021.
- [124] Y. Zheng, S. Bian, J. Sun, L. Wen, G. Rong, and M. Sawan, “Label-free lspr-vertical microcavity biosensor for on-site sars-cov-2 detection,” *Biosensors*, vol. 12, no. 3, p. 151, 2022.
- [125] Y. Yang, L. A. Wasiewska, C. M. Burgess, G. Duffy, P. Lovera, and A. O’Riordan, “Detection of stx2 from shiga toxin-producing escherichia coli (stec) by a surface enhanced raman spectroscopy (sers) sensor using recycled silicon chips,” *Sensors and Actuators B: Chemical*, vol. 373, p. 132618, 2022.
- [126] W. Zhao, J. Li, Z. Xue, X. Qiao, A. Li, X. Chen, Y. Feng, Z. Yang, and T. Wang, “A separation-sensing platform performing accurate diagnosis of jaundice in complex biological tear fluids,” *Angewandte Chemie*, vol. 134, no. 29, p. e202205628, 2022.
- [127] N. A. Mortensen and S. Xiao, “Slow-light enhancement of beer-lambert-bouguer absorption,” *Applied Physics Letters*, vol. 90, no. 14, p. 141108, 2007.
- [128] W.-C. Lai, S. Chakravarty, X. Wang, C. Lin, and R. T. Chen, “On-chip methane sensing by near-ir absorption signatures in a photonic crystal slot waveguide,” *Optics letters*, vol. 36, no. 6, pp. 984–986, 2011.
- [129] M. R. Bryan, J. N. Butt, J. Bucukovski, and B. L. Miller, “Biosensing with silicon nitride microring resonators integrated with an on-chip filter bank spectrometer,” *ACS sensors*, vol. 8, no. 2, pp. 739–747, 2023.
- [130] W.-C. Lai, S. Chakravarty, X. Wang, C. Lin, and R. T. Chen, “Photonic crystal slot waveguide absorption spectrometer for on-chip near-infrared spectroscopy of xylene in water,” *Applied Physics Letters*, vol. 98, no. 2, p. 7, 2011.
- [131] L. Tombez, E. Zhang, J. Orcutt, S. Kamlapurkar, and W. Green, “Methane absorption spectroscopy on a silicon photonic chip,” *Optica*, vol. 4, no. 11, pp. 1322–1325, 2017.

- [132] X. Guo, F. Zheng, C. Li, X. Yang, N. Li, S. Liu, J. Wei, X. Qiu, and Q. He, “A portable sensor for in-situ measurement of ammonia based on near-infrared laser absorption spectroscopy,” *Optics and Lasers in Engineering*, vol. 115, pp. 243–248, 2019.
- [133] X. Tan, H. Zhang, J. Li, H. Wan, Q. Guo, H. Zhu, H. Liu, and F. Yi, “Non-dispersive infrared multi-gas sensing via nanoantenna integrated narrowband detectors,” *Nature communications*, vol. 11, no. 1, pp. 1–9, 2020.
- [134] F. Ottonello-Briano, C. Errando-Herranz, H. Rödjegård, H. Martin, H. Sohlström, and K. B. Gylfason, “Carbon dioxide absorption spectroscopy with a mid-infrared silicon photonic waveguide,” *Optics Letters*, vol. 45, no. 1, pp. 109–112, 2020.
- [135] Q. Qiao, H. Sun, X. Liu, B. Dong, J. Xia, C. Lee, and G. Zhou, “Suspended silicon waveguide with sub-wavelength grating cladding for optical mems in mid-infrared,” *Micromachines*, vol. 12, no. 11, p. 1311, 2021.
- [136] A. Rostamian, J. Midkiff, K. M. Yoo, and R. T. Chen, “Slow light engineering in the hollow-core vertical photonic crystal waveguide for gas sensing,” in *CLEO: Applications and Technology*, pp. AW4L–6, Optica Publishing Group, 2022.
- [137] H. Dalir, R. T. Chen, M. H. Teimourpour, J. Midkiff, and A. Rostamian, “Vertical photonic crystal waveguide for gas detection,” Sept. 9 2021. US Patent App. 17/195,542.
- [138] Y. An, S. Jain, M. H. Hlaing, J. Midkiff, and R. T. Chen, “Highly efficient atmospheric gases detection using slow light effect induced in vertical photonic crystal waveguide arrays,” in *CLEO: Fundamental Science*, pp. JW2A–73, Optica Publishing Group, 2023.
- [139] N. Singh, A. Casas-Bedoya, D. D. Hudson, A. Read, E. Mägi, and B. J. Eggleton, “Mid-ir absorption sensing of heavy water using a silicon-on-sapphire waveguide,” *Optics Letters*, vol. 41, no. 24, pp. 5776–5779, 2016.
- [140] Y. Zou, S. Chakravarty, and R. T. Chen, “Mid-infrared silicon-on-sapphire waveguide coupled photonic crystal microcavities,” *Applied physics letters*, vol. 107, no. 8, p. 081109, 2015.
- [141] M. Vlk, A. Datta, S. Alberti, H. D. Yallev, V. Mittal, G. S. Murugan, and J. Jágorská, “Extraordinary evanescent field confinement waveguide sensor for mid-infrared trace gas spectroscopy,” *Light: Science & Applications*, vol. 10, no. 1, p. 26, 2021.
- [142] J. Wu, G. Yue, W. Chen, Z. Xing, J. Wang, W. R. Wong, Z. Cheng, S. Y. Set, G. Senthil Murugan, X. Wang, et al., “On-chip optical gas sensors based on group-iv materials,” *ACS photonics*, vol. 7, no. 11, pp. 2923–2940, 2020.
- [143] H. Amarloo and S. Safavi-Naeini, “Enhanced on-chip terahertz vibrational absorption spectroscopy using evanescent fields in silicon waveguide structures,” *Optics Express*, vol. 29, no. 11, pp. 17343–17352, 2021.
- [144] X. Wang, S.-S. Kim, R. Roßbach, M. Jetter, P. Michler, and B. Mizaikoff, “Ultra-sensitive mid-infrared evanescent field sensors combining thin-film strip waveguides with quantum cascade lasers,” *Analyst*, vol. 137, no. 10, pp. 2322–2327, 2012.
- [145] C. Xiong, Y. Martin, E. J. Zhang, J. S. Orcutt, M. Glodde, L. Schares, T. Barwicz, C. C. Teng, G. Wysocki, and W. M. Green, “Silicon photonic integrated circuit for on-chip spectroscopic gas sensing,” in *Silicon Photonics XIV*, vol. 10923, pp. 31–36, SPIE, 2019.
- [146] D. A. Irvine, V. Kilic, K. G. Petrillo, M. A. Foster, and A. C. Foster, “Evanescently coupled multimode silicon nitride waveguides for on chip spectroscopy,” in *2022 Conference on Lasers and Electro-Optics (CLEO)*, pp. 1–2, IEEE, 2022.
- [147] J. Zhou, D. A. Hussein, J. Li, Z. Lin, S. Sukhishvili, G. L. Cote, R. Gutierrez-Osuna, and P. T. Lin, “Mid-infrared serial microring resonator array for real-time detection of vapor-phase volatile organic compounds,” *Analytical Chemistry*, vol. 94, no. 31, pp. 11008–11015, 2022.
- [148] K. M. Yoo, J. Midkiff, A. Rostamian, C.-j. Chung, H. Dalir, and R. T. Chen, “InGaAs membrane waveguide: a promising platform for monolithic integrated mid-infrared optical gas sensor,” *ACS sensors*, vol. 5, no. 3, pp. 861–869, 2020.

- [149] B. Hinkov, F. Pilat, L. Lux, P. L. Souza, M. David, A. Schwaighofer, D. Ristanić, B. Schwarz, H. Detz, A. M. Andrews, et al., “A mid-infrared lab-on-a-chip for dynamic reaction monitoring,” *Nature communications*, vol. 13, no. 1, p. 4753, 2022.
- [150] S. Chakravarty, J. Midkiff, K. Yoo, A. Rostamian, and R. T. Chen, “Monolithic integration of quantum cascade laser, quantum cascade detector, and subwavelength waveguides for mid-infrared integrated gas sensing,” in *Quantum Sensing and Nano Electronics and Photonics XVI*, vol. 10926, pp. 204–211, SPIE, 2019.
- [151] B. Schwarz, P. Reininger, D. Ristanić, H. Detz, A. M. Andrews, W. Schrenk, and G. Strasser, “Monolithically integrated mid-infrared lab-on-a-chip using plasmonics and quantum cascade structures,” *Nature communications*, vol. 5, no. 1, p. 4085, 2014.
- [152] S. Jain, M. H. Hlaing, and R. T. Chen, “Wavelength tunable group delay in ingaas subwavelength grating waveguide for mid-infrared absorption spectroscopy,” in *CLEO: QELS\_Fundamental Science*, pp. JW3B–167, Optica Publishing Group, 2022.
- [153] J. Chai, K. Zhang, Y. Xue, W. Liu, T. Chen, Y. Lu, and G. Zhao, “Review of mems based fourier transform spectrometers,” *Micromachines*, vol. 11, no. 2, p. 214, 2020.
- [154] C. Liu, *Foundations of MEMS*. Pearson Education India, 2012.
- [155] B. Mortada, Y. M. Sabry, M. Nagi, K. Hassan, B. Saadany, T. Bourouina, and D. Khalil, “High-throughput deeplyetched scanning michelson interferometer on-chip,” in *2014 International Conference on Optical MEMS and Nanophotonics*, pp. 161–162, IEEE, 2014.
- [156] T. Sandner, A. Kenda, C. Drabe, H. Schenk, and W. Scherf, “Miniaturized ftr-spectrometer based on optical mems translatory actuator. in, vol. proc. spie 6466moems and miniaturized systems vi(pp. 646602e646612),” *International Society for Optics and Photonics*, 2007.
- [157] F. Merenda, S. Bühler, H. Farah, G. Boer, and T. Scharf, “Portable nir/mir fourier-transform spectrometer based on a common path lamellar grating interferometer,” in *Next-Generation Spectroscopic Technologies III*, vol. 7680, pp. 204–215, SPIE, 2010.
- [158] Y. Hongbin, Z. Guangya, C. F. Siong, L. Feiwen, W. Shouhua, and Z. Mingsheng, “An electromagnetically driven lamellar grating based fourier transform microspectrometer,” *Journal of Micromechanics and Microengineering*, vol. 18, no. 5, p. 055016, 2008.
- [159] A. Fathy, Y. M. Sabry, S. Nazeer, T. Bourouina, and D. A. Khalil, “On-chip parallel fourier transform spectrometer for broadband selective infrared spectral sensing,” *Microsystems & Nanoengineering*, vol. 6, no. 1, p. 10, 2020.
- [160] Q. Qiao, X. Liu, Z. Ren, B. Dong, J. Xia, H. Sun, C. Lee, and G. Zhou, “Mems-enabled on-chip computational mid-infrared spectrometer using silicon photonics,” *ACS Photonics*, vol. 9, no. 7, pp. 2367–2377, 2022.
- [161] M. Montesinos-Ballester, Q. Liu, V. Vakarín, J. M. Ramirez, C. Alonso-Ramos, X. L. Roux, J. Frigerio, A. Ballabio, E. Talamas, L. Vivien, et al., “On-chip fourier-transform spectrometer based on spatial heterodyning tuned by thermo-optic effect,” *Scientific Reports*, vol. 9, no. 1, p. 14633, 2019.
- [162] E. Le Coarer, S. Blaize, P. Benech, I. Stefanon, A. Morand, G. Léronnel, G. Leblond, P. Kern, J. M. Fedeli, and P. Royer, “Wavelength-scale stationary-wave integrated fourier-transform spectrometry,” *Nature Photonics*, vol. 1, no. 8, pp. 473–478, 2007.
- [163] X. Nie, E. Ryckeboer, G. Roelkens, and R. Baets, “Cmos-compatible broadband co-propagative stationary fourier transform spectrometer integrated on a silicon nitride photonics platform,” *Optics express*, vol. 25, no. 8, pp. A409–A418, 2017.
- [164] E. Heidari, X. Xu, C.-J. Chung, and R. T. Chen, “On-chip fourier transform spectrometer on silicon-on-sapphire,” *Optics Letters*, vol. 44, no. 11, pp. 2883–2886, 2019.
- [165] A. V. Velasco, P. Cheben, P. J. Bock, A. Delège, J. H. Schmid, J. Lapointe, S. Janz, M. L. Calvo, D.-X. Xu, M. Florjańczyk, et al., “High-resolution fourier-transform spectrometer chip with microphotonic silicon spiral waveguides,” *Optics letters*, vol. 38, no. 5, pp. 706–708, 2013.
- [166] S. N. Zheng, J. Zou, H. Cai, J. Song, L. Chin, P. Liu, Z. Lin, D. Kwong, and A. Q. Liu, “Microring resonator-assisted fourier transform spectrometer with enhanced resolution and large bandwidth in single chip solution,” *Nature communications*, vol. 10, no. 1, p. 2349, 2019.

- [167] K. M. Yoo and R. T. Chen, “Dual-polarization bandwidth-bridged bandpass sampling fourier transform spectrometer from visible to near-infrared on a silicon nitride platform,” *ACS photonics*, vol. 9, no. 8, pp. 2691–2701, 2022.
- [168] A. Li, C. Wang, F. Bao, W. Fang, Y. Liang, R. Cheng, and S. Pan, “An integrated single-shot spectrometer with large bandwidth-resolution ratio and wide operation temperature range,” *PhotoniX*, vol. 4, no. 1, p. 29, 2023.
- [169] D. M. Kita, B. Miranda, D. Favela, D. Bono, J. Michon, H. Lin, T. Gu, and J. Hu, “High-performance and scalable on-chip digital fourier transform spectroscopy,” *Nature communications*, vol. 9, no. 1, p. 4405, 2018.
- [170] H. Podmore, A. Scott, P. Cheben, A. V. Velasco, J. H. Schmid, M. Vachon, and R. Lee, “Demonstration of a compressive-sensing fourier-transform on-chip spectrometer,” *Optics letters*, vol. 42, no. 7, pp. 1440–1443, 2017.
- [171] K. M. Yoo, K.-C. Fan, M. Hlaing, S. Jain, S. Ning, Y. An, and R. T. Chen, “Lab-on-a-chip optical biosensor platform: a micro-ring resonator integrated with a near-infrared fourier transform spectrometer,” *Optics Letters*, vol. 48, no. 20, pp. 5371–5374, 2023.
- [172] K. M. Yoo, K.-C. Fan, Y. An, M. Hlaing, S. Jain, and R. T. Chen, “Near-infrared lab-on-a-chip optical biosensor with micro ring resonator and fourier transform spectrometer on soi platform,” in *CLEO: Science and Innovations*, pp. SF2E–1, Optica Publishing Group, 2023.
- [173] D. T. Cassidy and J. Reid, “Atmospheric pressure monitoring of trace gases using tunable diode lasers,” *Applied Optics*, vol. 21, no. 7, pp. 1185–1190, 1982.
- [174] D. T. Cassidy and L. J. Bonnell, “Trace gas detection with short-external-cavity ingaasp diode laser transmitter modules operating at 1.58  $\mu\text{m}$ ,” *Applied optics*, vol. 27, no. 13, pp. 2688–2693, 1988.
- [175] D. S. Bomse, A. C. Stanton, and J. A. Silver, “Frequency modulation and wavelength modulation spectroscopies: comparison of experimental methods using a lead-salt diode laser,” *Applied optics*, vol. 31, no. 6, pp. 718–731, 1992.
- [176] P. Kluczynski and O. Axner, “Theoretical description based on fourier analysis of wavelength-modulation spectrometry in terms of analytical and background signals,” *Applied optics*, vol. 38, no. 27, pp. 5803–5815, 1999.
- [177] H. Li, G. B. Rieker, X. Liu, J. B. Jeffries, and R. K. Hanson, “Extension of wavelength-modulation spectroscopy to large modulation depth for diode laser absorption measurements in high-pressure gases,” *Applied optics*, vol. 45, no. 5, pp. 1052–1061, 2006.
- [178] G. Wilson, “Modulation broadening of nmr and esr line shapes,” *Journal of Applied Physics*, vol. 34, no. 11, pp. 3276–3285, 1963.
- [179] R. Arndt, “Analytical line shapes for lorentzian signals broadened by modulation,” *Journal of Applied Physics*, vol. 36, no. 8, pp. 2522–2524, 1965.
- [180] J. Reid, B. Garside, J. Shewchun, M. El-Sherbiny, and E. Ballik, “High sensitivity point monitoring of atmospheric gases employing tunable diode lasers,” *Applied Optics*, vol. 17, no. 11, pp. 1806–1810, 1978.
- [181] J. Reid and D. Labrie, “Second-harmonic detection with tunable diode lasers—comparison of experiment and theory,” *Applied Physics B*, vol. 26, no. 3, pp. 203–210, 1981.
- [182] O. E. Myers and E. J. Putzer, “Measurement broadening in magnetic resonance,” *Journal of Applied Physics*, vol. 30, no. 12, pp. 1987–1991, 1959.
- [183] A. Russell and D. Torchia, “Harmonic analysis in systems using phase sensitive detectors,” *Review of Scientific Instruments*, vol. 33, no. 4, pp. 442–444, 1962.
- [184] A. Dharamsi, “A theory of modulation spectroscopy with applications of higher harmonic detection,” *Journal of Physics D: Applied Physics*, vol. 29, no. 3, p. 540, 1996.
- [185] M. H. Hlaing, P. Chinsuti, C. Azevedo, and A. Khan, “Modulation properties of mid-ir quantum cascade laser using higher-harmonic modulation spectroscopy,” in *Laser Science*, pp. JW3A–32, Optica Publishing Group, 2019.

- [186] E. A. Whittaker, C. M. Shum, H. Grebel, and H. Lotem, "Reduction of residual amplitude modulation in frequency-modulation spectroscopy by using harmonic frequency modulation," *JOSA B*, vol. 5, no. 6, pp. 1253–1256, 1988.
- [187] A. Hangauer, J. Chen, R. Strzoda, and M.-C. Amann, "Multi-harmonic detection in wavelength modulation spectroscopy systems," *Applied Physics B*, vol. 110, pp. 177–185, 2013.
- [188] M. Loewenstein, "Diode laser harmonic spectroscopy applied to in situ measurements of atmospheric trace molecules," *Journal of Quantitative Spectroscopy and Radiative Transfer*, vol. 40, no. 3, pp. 249–256, 1988.
- [189] K. Namjou, S. Cai, E. A. Whittaker, J. Faist, C. Gmachl, F. Capasso, D. L. Sivco, and A. Y. Cho, "Sensitive absorption spectroscopy with a room-temperature distributed-feedback quantum-cascade laser," *Optics letters*, vol. 23, no. 3, pp. 219–221, 1998.
- [190] R. M. Williams, J. F. Kelly, S. W. Sharpe, J. S. Hartman, C. F. Gmachl, F. Capasso, D. L. Sivco, J. N. Baillargeon, and A. Y. Cho, "Spectral and modulation performance of quantum cascade lasers with application to remote sensing," in *Application of Tunable Diode and Other Infrared Sources for Atmospheric Studies and Industrial Processing Monitoring II*, vol. 3758, pp. 11–22, SPIE, 1999.
- [191] C. R. Webster, G. J. Flesch, D. C. Scott, J. E. Swanson, R. D. May, W. S. Woodward, C. Gmachl, F. Capasso, D. L. Sivco, J. N. Baillargeon, et al., "Quantum-cascade laser measurements of stratospheric methane and nitrous oxide," *Applied Optics*, vol. 40, no. 3, pp. 321–326, 2001.
- [192] F. S. Pavone and M. Inguscio, "Frequency- and wavelength-modulation spectroscopies: comparison of experimental methods using an AlGaAs diode laser," *Applied Physics B*, vol. 56, pp. 118–122, 1993.
- [193] M. Gabrysch, C. Corsi, F. Pavone, and M. Inguscio, "Simultaneous detection of CO and CO<sub>2</sub> using a semiconductor DFB diode laser at 1.578  $\mu\text{m}$ ," *Applied Physics B*, vol. 65, pp. 75–79, 1997.
- [194] A. Lucchesini, C. Gabbanini, S. Gozzini, L. Moi, et al., "Diode laser spectroscopy of methane overtone transitions," *Applied Optics*, vol. 32, no. 27, pp. 5211–5216, 1993.
- [195] X. Zhu and D. T. Cassidy, "Modulation spectroscopy with a semiconductor diode laser by injection-current modulation," *JOSA B*, vol. 14, no. 8, pp. 1945–1950, 1997.
- [196] M. H. Hlaing, *Sensitive Detection of Atmospheric Methane and Nitrous Oxide Using Higher Harmonic Wavelength Modulation Spectroscopy*. Delaware State University, 2020.
- [197] M. Hlaing, C. Azevedo, and A. Khan, "Multi-harmonic wavelength modulation spectroscopy for the detection of atmospheric methane and nitrous oxide in mid-IR region," *Bulletin of the American Physical Society*, vol. 63, 2018.
- [198] L. Chen, Y. Shi, X. Zhu, W. Guo, M. Zhang, Y. Che, L. Tang, X. Yang, Q. You, and Z. Liu, "IL-10 secreted by cancer-associated macrophages regulates proliferation and invasion in gastric cancer cells via c-met/stat3 signaling," *Oncology reports*, vol. 42, no. 2, pp. 595–604, 2019.
- [199] Z. Du, J. Li, X. Cao, H. Gao, and Y. Ma, "High-sensitive carbon disulfide sensor using wavelength modulation spectroscopy in the mid-infrared fingerprint region," *Sensors and Actuators B: Chemical*, vol. 247, pp. 384–391, 2017.
- [200] S. Guo, J. Li, Y. Wei, Y. Yang, Z. Lu, X. Xing, W. Ren, and S. Yao, "A multi-laser hybrid absorption sensor for simultaneous measurement of NH<sub>3</sub>, NO, and temperature in denitrification flue gas," *Infrared Physics & Technology*, vol. 136, p. 105034, 2024.
- [201] J. Li, W. Ma, Z. Wang, Y. Zhou, L. He, M. Lin, and Y. Ji, "Miniaturized and portable laser gas sensor for standoff methane detection with non-cooperative targets," *Applied Spectroscopy*, vol. 78, no. 1, pp. 76–83, 2024.
- [202] G. Rieker, H. Li, X. Liu, J. Liu, J. Jeffries, R. Hanson, M. Allen, S. Wehe, P. Mulhall, H. Kindle, et al., "Rapid measurements of temperature and H<sub>2</sub>O concentration in IC engines with a spark plug-mounted diode laser sensor," *Proceedings of the Combustion Institute*, vol. 31, no. 2, pp. 3041–3049, 2007.
- [203] R. Wainner, B. Green, M. Allen, M. White, J. Stafford-Evans, and R. Naper, "Handheld, battery-powered near-IR TDL sensor for stand-off detection of gas and vapor plumes," *Applied Physics B*, vol. 75, pp. 249–254, 2002.
- [204] A. J. McGettrick, K. Duffin, W. Johnstone, G. Stewart, and D. G. Moodie, "Tunable diode laser spectroscopy with wavelength modulation: A phasor decomposition method for calibration-free



- measurements of gas concentration and pressure,” *Journal of Lightwave Technology*, vol. 26, no. 4, pp. 432–440, 2008.
- [205] C. Wang and P. Sahay, “Breath analysis using laser spectroscopic techniques: breath biomarkers, spectral fingerprints, and detection limits,” *Sensors*, vol. 9, no. 10, pp. 8230–8262, 2009.
- [206] H. Chu, Y. Ma, and L. Yang, “Wavelength modulation spectrometer using interband cascade laser for exhaled breath carbon monoxide measurement,” in *AOPC 2021: Infrared Device and Infrared Technology*, vol. 12061, pp. 331–334, SPIE, 2021.
- [207] M. R. McCurdy, Y. Bakhirkin, G. Wysocki, R. Lewicki, and F. K. Tittel, “Recent advances of laser-spectroscopybased techniques for applications in breath analysis,” *Journal of breath research*, vol. 1, no. 1, p. 014001, 2007.
- [208] M. Pi, Y. Huang, H. Zhao, Z. Peng, J. Lang, J. Ji, L. Teng, F. Song, L. Liang, Y. Zhang, et al., “Theoretical and experimental investigation of on-chip mid-infrared chalcogenide waveguide ch<sub>4</sub> sensor based on wavelength modulation spectroscopy,” *Sensors and Actuators B: Chemical*, vol. 362, p. 131782, 2022.
- [209] M. Pi, C. Zheng, H. Zhao, J. Ji, Z. Peng, Y. Min, Y. Huang, X. Wang, G. Guan, F. Song, et al., “Mid-infrared auto-correction on-chip waveguide gas sensor based on 2f/1f wavelength modulation spectroscopy,” *Optics Letters*, vol. 49, no. 2, pp. 190–193, 2024.
- [210] H. Zhao, C. Zheng, M. Pi, L. Liang, F. Song, K. Zheng, Y. Zhang, Y. Wang, and F. K. Tittel, “Wms-based nearinfrared on-chip acetylene sensor using polymeric su8 archimedean spiral waveguide with euler s-bend,” *Spectrochimica Acta Part A: Molecular and Biomolecular Spectroscopy*, p. 123020, 2023.
- [211] M. Kourogi, K. Nakagawa, and M. Ohtsu, “Wide-span optical frequency comb generator for accurate optical frequency difference measurement,” *IEEE Journal of Quantum Electronics*, vol. 29, no. 10, pp. 2693–2701, 1993.
- [212] J. Ye, L.-S. Ma, T. Daly, and J. L. Hall, “Highly selective terahertz optical frequency comb generator,” *Optics Letters*, vol. 22, no. 5, pp. 301–303, 1997.
- [213] D. J. Jones, S. A. Diddams, J. K. Ranka, A. Stentz, R. S. Windeler, J. L. Hall, and S. T. Cundiff, “Carrier-envelope phase control of femtosecond mode-locked lasers and direct optical frequency synthesis,” *Science*, vol. 288, no. 5466, pp. 635–639, 2000.
- [214] F.-L. Hong, K. Minoshima, A. Onae, H. Inaba, H. Takada, A. Hirai, H. Matsumoto, T. Sugiura, and M. Yoshida, “Broad-spectrum frequency comb generation and carrier-envelope offset frequency measurement by second-harmonic generation of a mode-locked fiber laser,” *Optics letters*, vol. 28, no. 17, pp. 1516–1518, 2003.
- [215] J. Rauschenberger, T. M. Fortier, D. J. Jones, J. Ye, and S. T. Cundiff, “Control of the frequency comb from a mode-locked erbium-doped fiber laser,” *Optics Express*, vol. 10, no. 24, pp. 1404–1410, 2002.
- [216] T. Udem, J. Reichert, R. Holzwarth, and T. Hänsch, “Accurate measurement of large optical frequency differences with a mode-locked laser,” *Optics letters*, vol. 24, no. 13, pp. 881–883, 1999.
- [217] H. R. Telle, G. Steinmeyer, A. E. Dunlop, J. Stenger, D. H. Sutter, and U. Keller, “Carrier-envelope offset phase control: A novel concept for absolute optical frequency measurement and ultrashort pulse generation,” *Applied Physics B*, vol. 69, pp. 327–332, 1999.
- [218] J. Reichert, R. Holzwarth, T. Udem, and T. W. Hänsch, “Measuring the frequency of light with mode-locked lasers,” *Optics communications*, vol. 172, no. 1-6, pp. 59–68, 1999.
- [219] S. A. Diddams, T. Udem, J. Bergquist, E. Curtis, R. Drullinger, L. Hollberg, W. M. Itano, W. Lee, C. Oates, K. Vogel, et al., “An optical clock based on a single trapped <sup>199</sup>Hg<sup>+</sup> ion,” *Science*, vol. 293, no. 5531, pp. 825–828, 2001.
- [220] T. Udem, R. Holzwarth, and T. W. Hänsch, “Optical frequency metrology,” *Nature*, vol. 416, no. 6877, pp. 233–237, 2002.
- [221] S. Bize, S. Diddams, U. Tanaka, C. Tanner, W. Oskay, R. E. Drullinger, T. Parker, T. P. Heavner, S. R. Jefferts, L. Hollberg, et al., “Testing the stability of fundamental constants with the <sup>199</sup>Hg<sup>+</sup> single-ion optical clock,” *Physical Review Letters*, vol. 90, no. 15, p. 150802, 2003.

- [222] R. K. Shelton, L.-S. Ma, H. C. Kapteyn, M. M. Murnane, J. L. Hall, and J. Ye, “Phase-coherent optical pulse synthesis from separate femtosecond lasers,” *Science*, vol. 293, no. 5533, pp. 1286–1289, 2001.
- [223] N. Picqué and T. W. Hänsch, “Frequency comb spectroscopy,” *Nature Photonics*, vol. 13, no. 3, pp. 146–157, 2019.
- [224] J. Ye, L. S. Ma, and J. L. Hall, “Molecular iodine clock,” *Physical Review Letters*, vol. 87, no. 27, p. 270801, 2001.
- [225] C. Lisdat, G. Grosche, N. Quintin, C. Shi, S. Raupach, C. Grebing, D. Nicolodi, F. Stefani, A. Al-Masoudi, S. Dörscher, et al., “A clock network for geodesy and fundamental science,” *Nature communications*, vol. 7, no. 1, p. 12443, 2016.
- [226] F. Ferdous, H. Miao, D. E. Leaird, K. Srinivasan, J. Wang, L. Chen, L. T. Varghese, and A. M. Weiner, “Spectral line-by-line pulse shaping of on-chip microresonator frequency combs,” *Nature Photonics*, vol. 5, no. 12, pp. 770–776, 2011.
- [227] H. R. Telle, B. Lipphardt, and J. Stenger, “Kerr-lens, mode-locked lasers as transfer oscillators for optical frequency measurements,” *Applied Physics B*, vol. 74, pp. 1–6, 2002.
- [228] J. Ye, L.-S. Ma, and J. L. Hall, “Ultrasensitive detections in atomic and molecular physics: demonstration in molecular overtone spectroscopy,” *JOSA B*, vol. 15, no. 1, pp. 6–15, 1998.
- [229] S. T. Cundiff and J. Ye, “Colloquium: Femtosecond optical frequency combs,” *Reviews of Modern Physics*, vol. 75, no. 1, p. 325, 2003.
- [230] S. McCall, “Whispering-gallery mode microdisk lasers,” *Appl. Phys. Lett.*, vol. 60, p. 20, 1991.
- [231] V. Braginsky, M. Gorodetsky, and V. Ilchenko, “Quality-factor and nonlinear properties of optical whispering-gallery modes,” *Physics letters A*, vol. 137, no. 7-8, pp. 393–397, 1989.
- [232] N. Bloembergen, “Nonlinear optics and spectroscopy,” *Reviews of Modern Physics*, vol. 54, no. 3, p. 685, 1982.
- [233] K. J. Vahala, “Optical microcavities,” *nature*, vol. 424, no. 6950, pp. 839–846, 2003.
- [234] Y.-W. Hu, Y.-F. Xiao, Y.-C. Liu, and Q. Gong, “Optomechanical sensing with on-chip microcavities,” *Frontiers of Physics*, vol. 8, pp. 475–490, 2013.
- [235] S. K. Manjeshwar, A. Ciers, J. Monsel, H. Pfeifer, C. Peralle, S. M. Wang, P. Tassin, and W. Wieczorek, “Integrated microcavity optomechanics with a suspended photonic crystal mirror above a distributed bragg reflector,” *arXiv preprint arXiv:2305.13511*, 2023.
- [236] X. Jiang, Q. Lin, J. Rosenberg, K. Vahala, and O. Painter, “High-q double-disk microcavities for cavity optomechanics,” *Optics express*, vol. 17, no. 23, pp. 20911–20919, 2009.
- [237] Y. K. Chembo, “Kerr optical frequency combs: theory, applications and perspectives,” *Nanophotonics*, vol. 5, no. 2, pp. 214–230, 2016.
- [238] C. Wang, M. Zhang, M. Yu, R. Zhu, H. Hu, and M. Loncar, “Monolithic lithium niobate photonic circuits for kerr frequency comb generation and modulation,” *Nature communications*, vol. 10, no. 1, p. 978, 2019.
- [239] A. L. Gaeta, M. Lipson, and T. J. Kippenberg, “Photonic-chip-based frequency combs,” *nature photonics*, vol. 13, no. 3, pp. 158–169, 2019.
- [240] B. Y. Kim, *Nonsoliton Kerr Combs*. Columbia University, 2022.
- [241] B. Chen, Y. Zhou, P. Huang, C. Ye, Q. Cao, Y. Liu, C. Kim, K. Yvind, J. Li, C. Dong, et al., “Integrated optical vortex microcomb,” *arXiv preprint arXiv:2212.07641*, 2022.
- [242] H. Weng, M. McDermott, A. A. Afridi, H. Tu, Q. Lu, W. Guo, and J. F. Donegan, “Turn-key kerr soliton generation and tunable microwave synthesizer in dual-mode  $\text{Si}_3\text{N}_4$  microresonators,” *Optics Express*, vol. 32, no. 3, pp. 3123–3137, 2024.
- [243] M. Karim, N. Al Kayed, R. Rafi, and B. Rahman, “Design and analysis of inverse tapered silicon nitride waveguide for flat and highly coherent supercontinuum generation in the mid-infrared,” *Optical and Quantum Electronics*, vol. 56, no. 1, p. 68, 2024.
- [244] M. Faisal, M. Karim, T. Shafiq, and B. Rahman, “Dispersion tailored suspended core  $\text{Si}_3\text{N}_4$  channel waveguide for broadband supercontinuum generation,” *Optical and Quantum Electronics*, vol. 56, no. 3, p. 351, 2024.

- [245] H. Wang, Q. Zeng, H. Ma, and Z. Yuan, "Progress on chip-based spontaneous four-wave mixing quantum light sources," *Advanced Devices & Instrumentation*, 2024.
- [246] M. R. Alizadeh, M. Seifouri, and S. Olyaei, "Numerical investigation of supercontinuum generation and optical frequency combs in sin-based pcf with high nonlinear coefficient," *Optoelectronics Letters*, vol. 20, no. 3, pp. 163–170, 2024.
- [247] T. Kippenberg, S. Spillane, and K. Vahala, "Kerr-nonlinearity optical parametric oscillation in an ultrahigh-q toroid microcavity," *Physical review letters*, vol. 93, no. 8, p. 083904, 2004.
- [248] M. H. Pfeiffer, C. Herkommer, J. Liu, H. Guo, M. Karpov, E. Lucas, M. Zervas, and T. J. Kippenberg, "Octavespanning dissipative kerr soliton frequency combs in  $\text{Si}_3\text{N}_4$  microresonators," *Optica*, vol. 4, no. 7, pp. 684–691, 2017.
- [249] Q. Li, T. C. Briles, D. A. Westly, T. E. Drake, J. R. Stone, B. R. Ilic, S. A. Diddams, S. B. Papp, and K. Srinivasan, "Stably accessing octave-spanning microresonator frequency combs in the soliton regime," *Optica*, vol. 4, no. 2, pp. 193–203, 2017.
- [250] P. Del'Haye, A. Coillet, T. Fortier, K. Beha, D. C. Cole, K. Y. Yang, H. Lee, K. J. Vahala, S. B. Papp, and S. A. Diddams, "Phase-coherent microwave-to-optical link with a self-referenced microcomb," *Nature Photonics*, vol. 10, no. 8, pp. 516–520, 2016.
- [251] A. A. Savchenkov, A. B. Matsko, D. Strekalov, M. Mohageg, V. S. Ilchenko, and L. Maleki, "Low threshold optical oscillations in a whispering gallery mode  $c a f 2$  resonator," *Physical review letters*, vol. 93, no. 24, p. 243905, 2004.
- [252] S. B. Papp, K. Beha, P. Del'Haye, F. Quinlan, H. Lee, K. J. Vahala, and S. A. Diddams, "Microresonator frequency comb optical clock," *Optica*, vol. 1, no. 1, pp. 10–14, 2014.
- [253] P. Del'Haye, O. Arcizet, M. L. Gorodetsky, R. Holzwarth, and T. J. Kippenberg, "Frequency comb assisted diode laser spectroscopy for measurement of microcavity dispersion," *Nature photonics*, vol. 3, no. 9, pp. 529–533, 2009.
- [254] M.-G. Suh, Q.-F. Yang, K. Y. Yang, X. Yi, and K. J. Vahala, "Microresonator soliton dual-comb spectroscopy," *Science*, vol. 354, no. 6312, pp. 600–603, 2016.
- [255] A. Dutt, C. Joshi, X. Ji, J. Cardenas, Y. Okawachi, K. Luke, A. L. Gaeta, and M. Lipson, "On-chip dual-comb source for spectroscopy," *Science advances*, vol. 4, no. 3, p. e1701858, 2018.
- [256] P. Marin-Palomo, J. N. Kemal, M. Karpov, A. Kordts, J. Pfeifle, M. H. Pfeiffer, P. Trocha, S. Wolf, V. Brasch, M. H. Anderson, et al., "Microresonator-based solitons for massively parallel coherent optical communications," *Nature*, vol. 546, no. 7657, pp. 274–279, 2017.
- [257] M.-G. Suh and K. J. Vahala, "Soliton microcomb range measurement," *Science*, vol. 359, no. 6378, pp. 884–887, 2018.
- [258] Y. Okawachi, K. Saha, J. S. Levy, Y. H. Wen, M. Lipson, and A. L. Gaeta, "Octave-spanning frequency comb generation in a silicon nitride chip," *Optics letters*, vol. 36, no. 17, pp. 3398–3400, 2011.
- [259] A. G. Griffith, R. K. Lau, J. Cardenas, Y. Okawachi, A. Mohanty, R. Fain, Y. H. D. Lee, M. Yu, C. T. Phare, C. B. Poitras, et al., "Silicon-chip mid-infrared frequency comb generation," *Nature communications*, vol. 6, no. 1, p. 6299, 2015.
- [260] H. Jung, R. Stoll, X. Guo, D. Fischer, and H. X. Tang, "Green, red, and ir frequency comb line generation from single ir pump in aln microring resonator," *Optica*, vol. 1, no. 6, pp. 396–399, 2014.
- [261] M. Pu, L. Ottaviano, E. Semenova, and K. Yvind, "Efficient frequency comb generation in algaas-on-insulator," *Optica*, vol. 3, no. 8, pp. 823–826, 2016.
- [262] G. Guan, A. Liu, C. Zheng, M. Pi, K. Zheng, B. Zhu, X. Wu, J. Zheng, Y. Wang, and F. K. Tittel, "Numerical investigation of on-chip multi-gas sensing using a low-repetition-frequency microcavity kerr comb with backward interference structure," *Journal of Lightwave Technology*, 2023.
- [263] H. Zhao, C. Zheng, M. Pi, L. Liang, F. Song, Y. Zhang, Y. Wang, and F. K. Tittel, "On-chip mid-infrared silicon-on-insulator waveguide methane sensor using two measurement schemes at  $3.291 \mu\text{m}$ ," *Frontiers in Chemistry*, vol. 10, p. 953684, 2022.
- [264] M. Yu, Y. Okawachi, A. G. Griffith, M. Lipson, and A. L. Gaeta, "Microfluidic mid-infrared spectroscopy via microresonator-based dual-comb source," *Optics Letters*, vol. 44, no. 17, pp. 4259–4262, 2019.

- [265] M. Pi, C. Zheng, H. Zhao, Z. Peng, G. Guan, J. Ji, Y. Huang, Y. Min, L. Liang, F. Song, et al., “Ultra-wideband mid-infrared chalcogenide suspended nanorib waveguide gas sensors with exceptionally high external confinement factor beyond free-space,” *ACS nano*, vol. 17, no. 18, pp. 17761–17770, 2023.
- [266] M. Yu, Y. Okawachi, A. G. Griffith, N. Picqué, M. Lipson, and A. L. Gaeta, “Silicon-chip-based mid-infrared dualcomb spectroscopy,” *Nature communications*, vol. 9, no. 1, p. 1869, 2018.
- [267] R. Bi, M. Pi, C. Zheng, H. Zhao, L. Liang, F. Song, D. Wang, Y. Zhang, Y. Wang, and F. K. Tittel, “A niobium pentoxide waveguide sensor for on-chip mid-infrared absorption spectroscopic methane measurement,” *Sensors and Actuators B: Chemical*, vol. 382, p. 133567, 2023.
- [268] E. van Doremale, X. Ji, J. Rivnay, and Y. van de Burgt, “A retrainable neuromorphic biosensor for on-chip learning and classification,” *Nature Electronics*, vol. 6, no. 10, pp. 765–770, 2023.
- [269] Y. Liang and J.-Y. Yoon, “In situ sensors for blood-brain barrier (bbb) on a chip,” *Sensors and Actuators Reports*, vol. 3, p. 100031, 2021.
- [270] S. Ren, S. Chen, H. Xu, X. Hou, Q. Yang, G. Wang, and C. Shen, “Unsupervised representation learning-based spectrum reconstruction for demodulation of fabry-perot interferometer sensor,” *IEEE Sensors Journal*, 2023.
- [271] T.-C. Liang, Y.-C. Chang, Z. Zhong, Y. Bigdeli, T.-Y. Ho, K. Chakrabarty, and R. Fair, “Dynamic adaptation using deep reinforcement learning for digital microfluidic biochips,” *ACM Transactions on Design Automation of Electronic Systems*, 2023.
- [272] W. Rawat and Z. Wang, “Deep convolutional neural networks for image classification: A comprehensive review,” *Neural computation*, vol. 29, no. 9, pp. 2352–2449, 2017.
- [273] H. Yu, L. T. Yang, Q. Zhang, D. Armstrong, and M. J. Deen, “Convolutional neural networks for medical image analysis: state-of-the-art, comparisons, improvement and perspectives,” *Neurocomputing*, vol. 444, pp. 92–110, 2021.
- [274] F. M. Khan, R. Gupta, and S. Sekhri, “A convolutional neural network approach for detection of e. coli bacteria in water,” *Environmental Science and Pollution Research*, vol. 28, no. 43, pp. 60778–60786, 2021.
- [275] J. Zhou, Z. Zhang, B. Dong, Z. Ren, W. Liu, and C. Lee, “Midinfrared spectroscopic analysis of aqueous mixtures using artificial-intelligence-enhanced metamaterial waveguide sensing platform,” *ACS nano*, vol. 17, no. 1, pp. 711–724, 2022.
- [276] Z. Xu, K. Wang, M. Zhang, T. Wang, X. Du, Z. Gao, S. Hu, X. Ren, and H. Feng, “Machine learning assisted dual-emission fluorescence/colorimetric sensor array detection of multiple antibiotics under stepwise prediction strategy,” *Sensors and Actuators B: Chemical*, vol. 359, p. 131590, 2022.
- [277] J. Zhang, P. Srivatsa, F. H. Ahmadzai, Y. Liu, X. Song, A. Karpatne, Z. Kong, and B. N. Johnson, “Reduction of biosensor false responses and time delay using dynamic response and theory-guided machine learning,” *ACS sensors*, 2023.
- [278] H. M. Robison, C. A. Chapman, H. Zhou, C. L. Erskine, E. Theel, T. Peikert, C. S. Lindestam Arlehamn, A. Sette, C. Bushell, M. Welge, et al., “Risk assessment of latent tuberculosis infection through a multiplexed cytokine biosensor assay and machine learning feature selection,” *Scientific reports*, vol. 11, no. 1, p. 20544, 2021.
- [279] C. Zhang, S. Bengio, M. Hardt, B. Recht, and O. Vinyals, “Understanding deep learning (still) requires rethinking generalization,” *Communications of the ACM*, vol. 64, no. 3, pp. 107–115, 2021.
- [280] J. Huang, T. Shi, B. Gong, X. Li, G. Liao, and Z. Tang, “Fitting an optical fiber background with a weighted savitzky–golay smoothing filter for raman spectroscopy,” *Applied Spectroscopy*, vol. 72, no. 11, pp. 1632–1644, 2018.
- [281] J. Zhang, P. Srivatsa, F. H. Ahmadzai, Y. Liu, X. Song, A. Karpatne, Z. J. Kong, and B. N. Johnson, “Improving biosensor accuracy and speed using dynamic signal change and theory-guided deep learning,” *Biosensors and Bioelectronics*, p. 115829, 2023.
- [282] G. Rong, Y. Xu, and M. Sawan, “Machine learning techniques for effective pathogen detection based on resonant biosensors,” *Biosensors*, vol. 13, no. 9, p. 860, 2023.
- [283] S. Hamed, H. D. Jahromi, and A. Lotfiani, “Artificial intelligence-aided nanoplasmonic biosensor modeling,” *Engineering Applications of Artificial Intelligence*, vol. 118, p. 105646, 2023.

- [284] T. Wang, S.-Y. Ma, L. G. Wright, T. Onodera, B. C. Richard, and P. L. McMahon, "An optical neural network using less than 1 photon per multiplication," *Nature Communications*, vol. 13, no. 1, p. 123, 2022.
- [285] L. Bernstein, A. Sludds, C. Panuski, S. Trajtenberg-Mills, R. Hamerly, and D. Englund, "Single-shot optical neural network," *Science Advances*, vol. 9, no. 25, p. eadg7904, 2023.
- [286] J. Gu, C. Feng, H. Zhu, R. T. Chen, and D. Z. Pan, "Light in ai: Toward efficient neurocomputing with optical neural networks-a tutorial," *IEEE Transactions on Circuits and Systems II: Express Briefs*, 2022.
- [287] C. Feng, J. Gu, H. Zhu, S. Ning, R. Tang, M. Hlaing, J. Midkiff, S. Jain, D. Z. Pan, and R. T. Chen, "Integrated multi-operand optical neurons for scalable and hardware-efficient deep learning," *Nanophotonics*, no. 0, 2024.
- [288] N. T. Pham, M. Bunruangses, P. Youplao, A. Garhwal, K. Ray, A. Roy, S. Boonkirdram, P. Yupapin, M. A. Jalil, J. Ali, et al., "An exploratory simulation study and prediction model on human brain behavior and activity using an integration of deep neural network and biosensor rabi antenna," *Heliyon*, vol. 9, no. 5, 2023.
- [289] C. Teng, X. Tang, Y. Huang, W. Du, W. He, A. Ren, J. Wu, and Z. Wang, "A high-stability all-optical nonlinear activator for optical computing," *Journal of Lightwave Technology*, 2023.